*Economic Geology,* v. 106, pp. 751–780

# Marble-Hosted Submicroscopic Gold Mineralization at Asimotrypes Area, Mount Pangeon, Southern Rhodope Core Complex, Greece

Demetrios G. Eliopoulos[1] and Stephanos P. Kilias[2,†]

[1] *Institute of Geology and Mineral Exploration (I.G.M.E.) Entrance C', 1 Sp. Louis Str., Olympic Village, GR-13677, Acharnae, Greece*

[2] *Department of Geology and Geoenvironment, National and Kapodistrian University of Athens, Athens 157 84, Greece*

## Abstract

Gold mineralization at Asimotrypes, Mount Pangeon, Greece, occurs within amphibolite facies rocks of the Southern Rhodope Core Complex, one of the largest metamorphic core complexes in the world. Exhumation of the complex resulted from middle Eocene to middle Miocene northeast-southwest–oriented extension in the northern Aegean and was controlled by the Kerdylion detachment zone. Host rocks are mylonitic, impure dolomite marbles of marine provenance ($\delta^{13}C$ = 1.9 – 2.9‰), which are intercalated with paramica schists, and amphibolites, and intruded by early Miocene syntectonic granitoids. In the Asimotrypes area, metamorphic rocks and granitoids exhibit flat mylonite-type ductile fabrics with consistent top-to-the-southwest sense of shear, as does the entire Complex.

Two mineralogically similar and spatially coincident gold mineralization styles, with a supergene overprint, exist: (1) strata-bound replacement bodies that contain up to 17 ppm gold, concentrated at and controlled by the intersections of several hydrothermally altered top-to-the-southwest marble mylonites, with crosscutting northwest-southeast to east-west–trending high-angle brittle normal faults and fractures, and (2) structurally controlled quartz veins, pods, and lenses with 4 to 13 ppm gold, which occur along the northwest-oriented subvertical brittle structures; the latter crosscut the ductile shear foliation of the host rocks, together with the granitoids, and dip steeply to the southwest. Gold-bearing replacement bodies typically occur as discordant wide halo adjacent to the centrally located brittle structures. Ductile top-to-the-southwest shear zones and crosscutting brittle structures are considered contemporaneous within the regional extensional deformation and exhumation history of the core complex host rocks. The distribution of gold mineralization is related to the geometry of the brittle structures, strongly suggesting that faults acted as major fluid feeder conduits during gold mineralization.

Hydrothermal alteration associated with the auriferous bodies and veins, overprinting the metamorphic rocks at Asimotrypes, consists of quartz, muscovite (sericite), chlorite, calcite (dedolomite), and sulfide minerals (locally, as much as 35 vol %). Gangue quartz occurs as (1) peripheral banded quartz with mylonitic texture, (2) dominant gold-bearing jasperoidal quartz, and (3) late, fine drusy quartz. The gold assemblage consists of arsenopyrite (41.7–43 wt % As; electron microprobe analyses) and arsenian pyrite encompassed by jasperoidal quartz; chalcopyrite, galena, tetrahedrite-tennantite, and sphalerite are trace phases. Secondary ion mass spectrometry (SIMS) spot analyses revealed that gold in replacement ore is submicroscopic and occurs in arsenopyrite and arsenian pyrite (As = 0.01–3.8 wt %), ranging from 0.5 to 29 ppm (mean = 11.6 ppm), and 0.14 to 11 ppm (mean = 2.3 ppm), respectively. Supergene overprint includes colloidal goethite + hematite containing native gold grains (size range, 20–40 $\mu$m) and lesser covellite, malachite, cerrussite, and chrysocolla. SIMS analysis also shows a primary, inhomogeneous distribution pattern for gold that appears to mimic finely banded growth twinning lamellae or growth zones. The form of the vein-related gold is unknown.

Fluid inclusions trapped during gold mineralization are low to medium salinity (<10 wt % NaCl equiv), aqueous-carbonic $H_2O$-$CO_2$-NaCl inclusions with highly variable carbonic to aqueous contents and naturally decrepitated or reequilibrated inclusions, interpreted to represent decompression by concurrent exhumation of the Southern Rhodope Core Complex. Trail-bound aqueous $H_2O$-NaCl inclusions are interpreted as a late extensional brittle deformation-related hydrothermal event unrelated to gold-bearing sulfide precipitation. Trapping temperatures of the $H_2O$-$CO_2$-NaCl inclusions and oxygen isotope equilibrium temperatures between quartz and muscovite (sericite) indicate formation of gold-bearing arsenopyrite, arsenian pyrite, and quartz bodies at ~270°C, with pressures of 1,800 to 2,000 bars corresponding to depths between 6 and 9 km under lithostatic load.

Measured hydrogen and calculated oxygen isotope compositions of the aqueous-carbonic mineralizing fluids ($\delta D_{water}$ = –125 to –105‰, $\delta^{18}O_{water}$ = 11.9 to 13.7 ‰ at 250°C, and 13.9 and 15.7 ‰ at 300°C) indicate an evolved meteoric origin. Water/rock calculations indicate these values could derive from heated meteoric water that had undergone isotope exchange during circulation through marbles at low water/rock ratio. Gold-associated sulfide minerals have $\delta^{34}S$ values between 2.2 and 3.1 per mil, interpreted as leaching of the core complex Paleozoic marine metasedimentary (marble), and interlayered mafic metavolcanic (amphibolites) and Miocene granitic rocks through fluid/rock interaction. Gold was probably precipitated from an $H_2S$-rich fluid when the host sulfide minerals were stabilized by pyritization of marble wall rock. Asimotrypes gold mineralization is interpreted as postmetamorphic and postmagmatic, and linked to late stages of exhumation of the Complex by middle Eocene to middle Miocene extension in the northern Aegean. The location and

† Corresponding author: e-mail, kilias@geol.uoa.gr


*Submitted: May 31, 2009*
*Accepted: March 22, 2011*

shape of gold orebodies are controlled by interactive ductile-then-brittle deformation, fluid flow and fluid-marble interaction processes. High paleogeothermal gradients associated with extension may have driven the dominantly meteoric fluid circulation downward within the exhuming Complex. Asimotrypes may represent a potential new gold mineralization style for the Rhodope region.

## Introduction

THE ASIMOTRYPES is an example of carbonate-hosted, submicroscopic gold mineralization, hosted by the Southern Rhodope Core Complex (Fig. 1), a recently recognized globally important example of extensional exhumation of metamorphic core complex (Dinter and Royden, 1993; Sokoutis et al., 1993; Dinter, 1998; Brun and Sokoutis, 2007). It is part of the Rhodope Massif and the Oligocene-Miocene Serbomacedonian-Rhodope magmatic and metallogenic belt. This belt is a classic area of gold mineralization and forms part of the Alpine-Balkan-Carpathian-Dinaride (ABCD) orogen and the great Tethyan-Eurasian metallogenic belt (Heinrich and Neubauer, 2002; Marchev et al., 2005). Recent studies in the Rhodope region (Heinrich and Neubauer, 2002; Lips, 2002; Kaiser-Rohrmeier et al., 2004; Marchev et al., 2005; Rice et al., 2007; Marton et al., 2010) have revealed close genetic relationships between hydrothermal ore formation, regional geodynamic evolution, postorogenic extensional magmatism, and detachment-related core complex formation.

The Asimotrypes gold mineralization lies between 1,200 and 1,300 m in the northeastern part of Mount Pangeon (1,956 m), 40 km west-southwest of Kavala (Fig. 1), in northeastern Greece. Mount Pangeon constitutes one of the most prominent gold mining districts of antiquity (e.g., Sagui, 1930). Numerous historical adits decorate Mount Pangeon (Sagui, 1930), and the overall tonnage of historical slag heaps in the broader area around Asimotrypes was estimated to be on the order of tens of thousands of tonnes (Higgins and Higgins, 1996). There is no total resource estimate for Asimotrypes. Exploration of the area for gold ore was carried out in 1977 by Bauxite Parnassus Mining Co. S.A. (today, S&B S.A.) with surface and adit investigations at the site of ancient workings (Fig. 2), but the area was abandoned as uneconomic. Two exploration adits of 109 m (3K-D) and 83 m (3K-H) lengths have been developed at the locations of ancient workings at Asimotrypes, at elevation ~1,250 m (Figs. 2, 3), providing good exposure to different styles of mineralization and host rocks within the gold mineralization system.

This paper reports geological, geochemical, mineralogical, fluid inclusion, and O, H, C, and S isotope data from Asimotrypes mineralization bodies and host rocks. These data are discussed in the context of the most recent geodynamic and tectonic framework for the Rhodope and northern Aegean, as one of the most active and prominent present-day continental extensional settings in the world. The data are

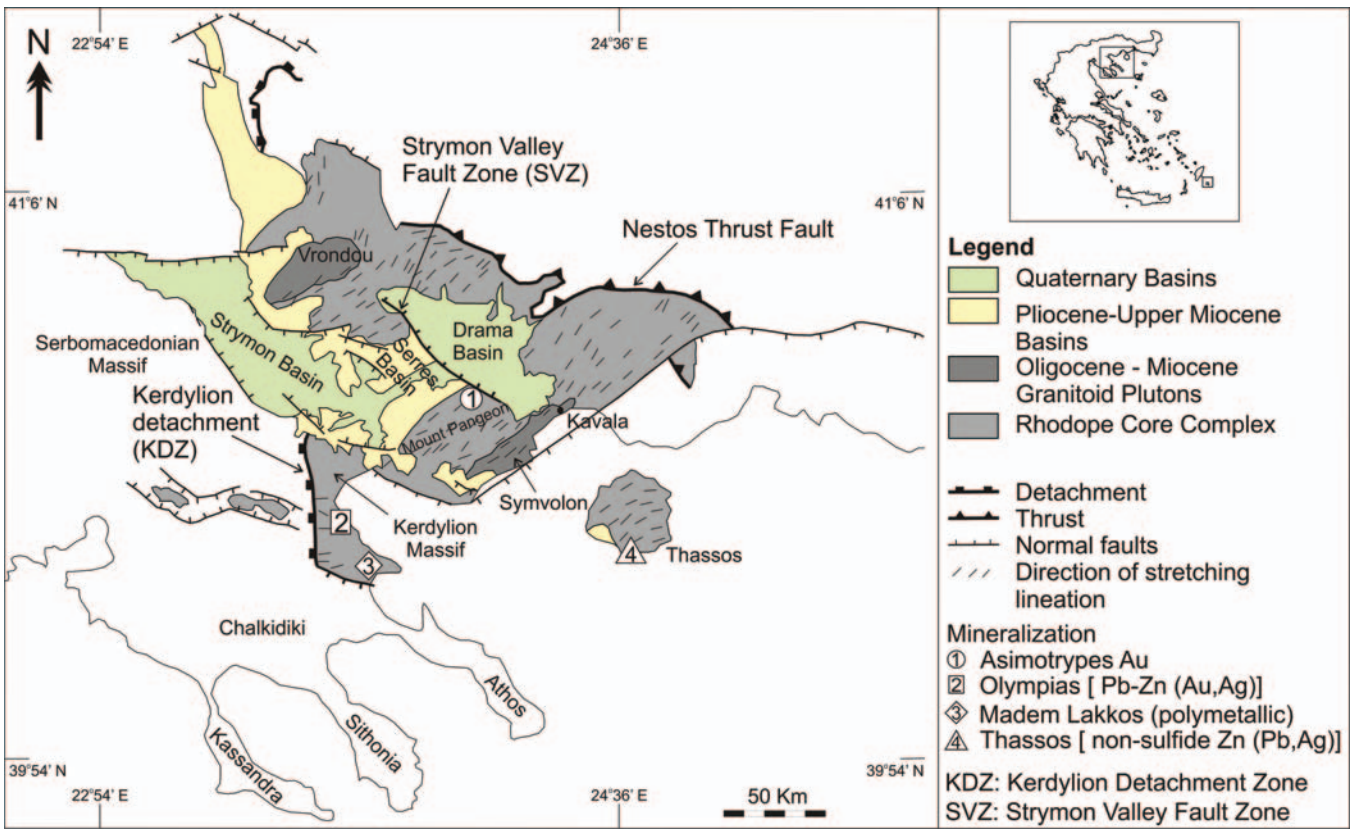


FIG. 1. Simplified geologic map of the Southern Rhodope Core Complex with main tectonic elements (after Brun and Sokoutis, 2007) and location of metallic deposits.

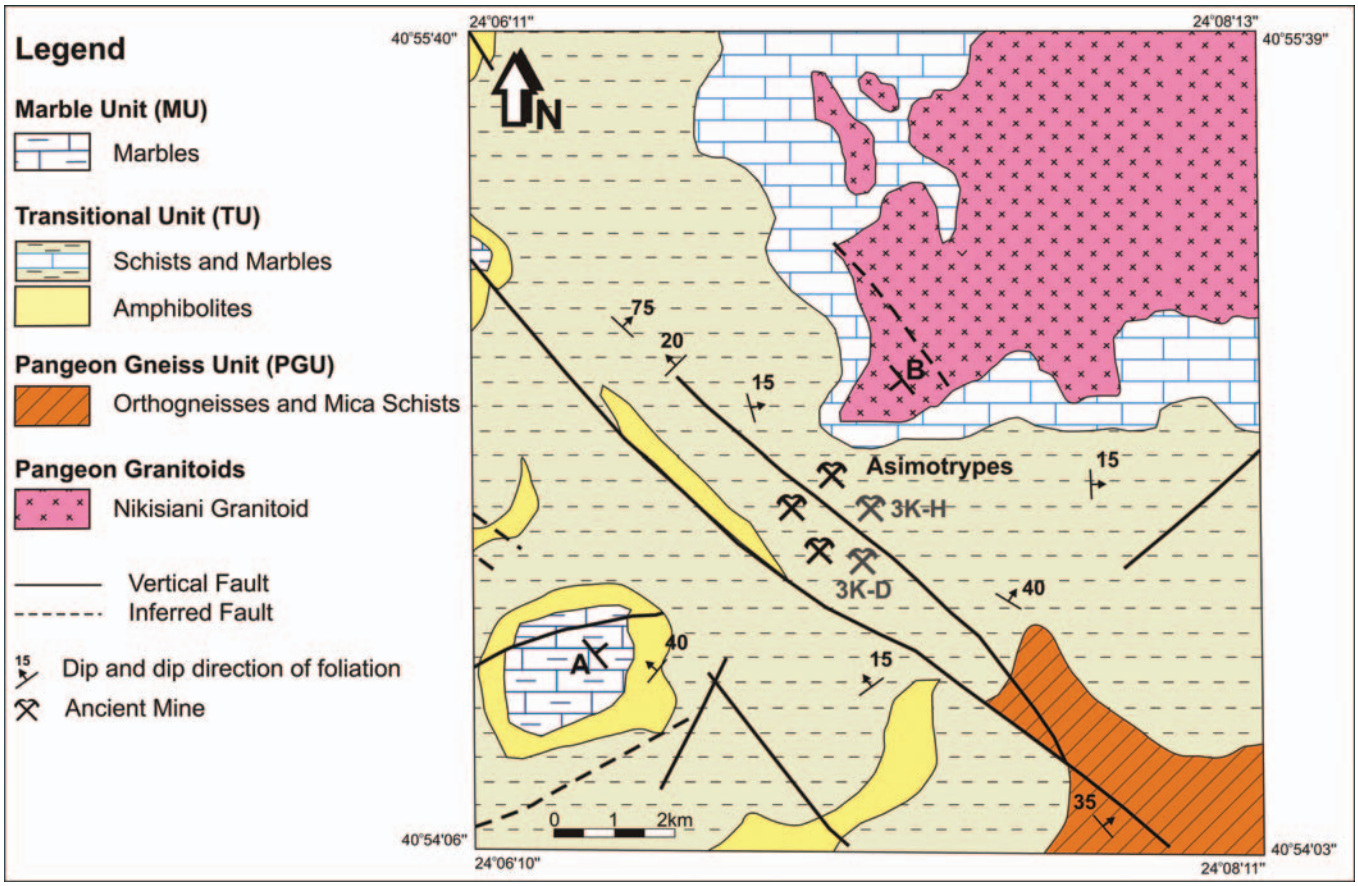


FIG. 2. Geologic map of the northeastern part of the Mount Pangeon showing the location of Asimotrypes area (modified after Xidas, 1984).

interpreted to suggest a new style of gold mineralization linked to regional extension and exhumation of the Southern Rhodope Core Complex.

## Sampling and Analytical Methods

Samples were collected from numerous field exposures and the two accessible adits. Secondary ion mass spectrometry (SIMS) spot analyses were carried out at the Advanced Mineral Technology Laboratory Limited, Canada, using an upgraded Cameca IMS–3f ion microprobe with an integrated image analysis system and using a primary beam of positive cesium ions. Molecular interference was eliminated by voltage offsetting (Chryssoulis et al., 1989). The instrument was calibrated using gold-implanted pyrite and arsenopyrite. The results were standardized with mineral specific calibration curves produced from the gold-implanted sulfide minerals (Chryssoulis et al., 1989).

Bulk rock geochemical analyses on mineralized samples and host rocks were carried out by the Institute of Geology and Mineral Exploration, Athens, Greece, Intertek Caleb Brett Ltd., UK (Au, Ag), and OMAC Laboratories Ltd., Ireland (Se, Te, Bi, Sb). All analyses were performed using inductively coupled plasma atomic emission spectrometry (ICP-AES), except for Se, Te, Bi, and Sb, for which atomic absorption spectroscopy (AAS) was used.

Microthermometric work was undertaken on doubly polished plates using a Linkam THSM 600 heating-freezing stage at IGME, Athens. The stage was attached to a Leitz Ortholux microscope carrying a Nikon Plan 40 long working distance objective. Calibration of the stage was done by using the melting point of pure $CO_2$ (–56.6°C) in a natural sample and commercial standards. Accuracy is estimated at ±0.5°C (between –100° and –20°C), ±0.2 °C (between –20° and +30°C), ±1°C (30°–200°C) and ±5°C (200°–500°C). Fluid inclusion compositions were calculated with the computer program developed by Bakker (2003), using the appropriate equations of state for aqueous (Zhang and Frantz, 1987), aqueous-carbonic (Bowers and Helgeson, 1983; Duschek et al., 1990; Duan et al., 1992; Bakker, 1999), and carbonic fluid inclusions (Span and Wagner, 1996). Fluid inclusion isochores were calculated from bulk density calculations based on microthermometric data, using the equations of state according to Span and Wagner (1996) in the pure $CO_2$ system, Bakker (1999) and Bowers and Helgeson (1983) in the $H_2O$-$CO_2$-NaCl system, and Zhang and Frantz (1987) in the $H_2O$-NaCl system.

Analyses of gases extracted from fluid inclusions were done at the British Geological Survey. Samples were selected on the basis of the abundance of apparently primary fluid inclusions. Fluid inclusion extracts produced by thermal decrepitation at 550°C under vacuum of cleaned quartz grains (9 samples) were analyzed using a purpose-built extraction line linked to a VG Micromass gas source quadrapole mass spectrometer (Shepherd et al., 1985). This is a bulk analysis method, and the values obtained are a mixture of the fluids

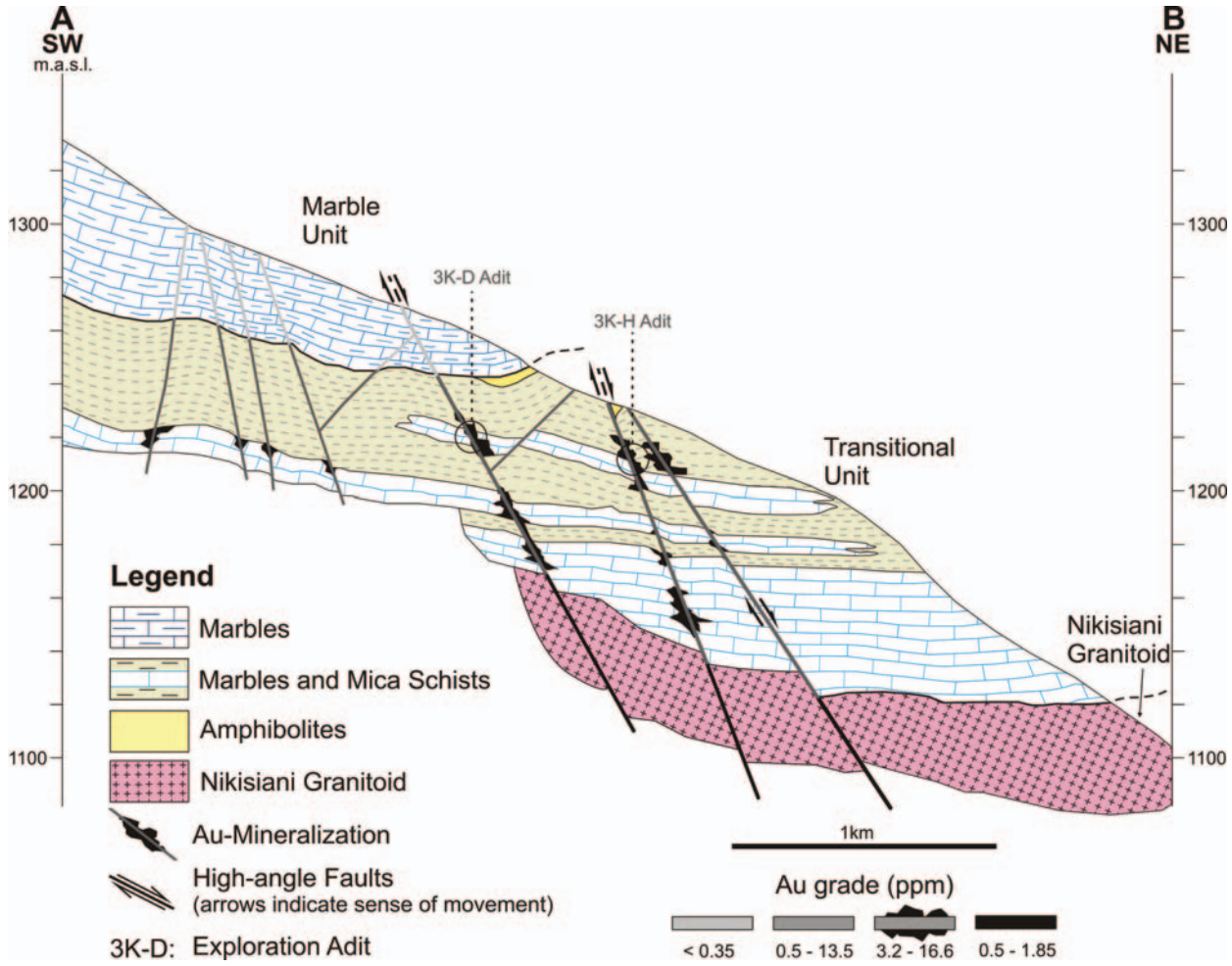


FIG. 3. Generalized southwest-northeast geologic cross section (A-B in Fig. 2) through the Asimotrypes area, northeastern Mount Pangeon, highlighting the stratigraphic and structural controls on gold mineralization, and gold grade distribution (Au grade). Note that the highest gold grades are restricted to the Transitional unit at intersections of subhorizontal marble horizons of the Transition unit with crosscutting northwest-southeast high-angle brittle normal faults. The depicted geologic relationships suggest that crosscutting northwest-oriented brittle faulting was a significant gold mineralization control. The interpretation is based on surface geology (modified after Nitsopoulos, 1980); m.a.s.l. = meters above sea level.

that were trapped during host quartz formation. There is also a minor contribution from fluids trapped in secondary fluid inclusions.

Sulfide mineral separates were analyzed for their sulfur isotope composition relative to Canyon Diablo troilite (V-CDT), on a VG 602D isotope ratio mass spectrometer at the Centre des Recherches Petrographic et Geochimiques, Nancy, France, with a precision of better than ± 0.2 per mil. The mass spectrometer was calibrated periodically against the five standards of Monster and Rees (1975).

Calcites from ore-hosting marbles were analyzed for their $\delta^{18}O$ at the University of Utrecht, using XRD on powdered carbonate samples that had been characterized by the relative percentages of calcite, dolomite, and other carbonate types. Samples were reacted with 100 percent phosphoric acid at 25°C, according to the method of McCrea (1950). Pure calcites, with less than 5 vol percent dolomite, were reacted overnight, and mixtures of calcite and dolomite were reacted for about 2 h, after which calcite $CO_2$ was extracted. Oxygen isotopes are related to Vienna-Standard Mean Ocean Water (V-SMOW) and were measured with a precision of ± 0.2 per mil or better.

Quartz and muscovite mineral separates were analyzed for $\delta^{18}O$ at the CSIRO Petroleum Resources Laboratory in Australia, following the method of Clayton and Mayeda (1963), with a precision ±0.15 per mil. All oxygen isotopes are related to the V-SMOW.

D/H isotopic analyses of inclusion fluids from auriferous quartz were performed at the CSIRO Petroleum Resources Laboratory in Australia, following a modified method published by Bigeleisen et al. (1952). The samples were heated to >800°C, using an RF generator furnace. $H_2$ produced was converted to $H_2O$ by contact with $CuO_2$ at 600°C. All water was collected cryogenically and stored in sealed 6-mm (outer diameter) borosilicate glass tubes. The water was released from the sealed tubes in a vacuum line and circulated using a pump through depleted uranium at 800°C to convert to $H_2$. When conversion was complete, the $H_2$ was pumped into the

mass spectrometer via a stainless steel line and analyzed immediately with a precision better than ±4 per mil. Analyses are reported in per mil relative to the V-SMOW.

In order to distinguish the carbonate mineral phases of ferroan calcite, dolomite, and ferroan dolomite, samples were treated with a solution of alizarin red S and potassium ferricyanide dissolved in dilute hydrochloric acid (Hitzman, 1999).

## Regional Geologic and Metallogenic Framework

The high-grade crystalline Rhodope Massif constitutes a crustal-scale accretionary wedge of metamorphic stacked nappes that is part of the Alpine-Himalayan orogen in the northern Aegean region and includes parts of southern Bulgaria and northern Greece (e.g., Burg et al., 1996; Gautier et al., 1999). It is composed of mainly Paleozoic continental material with intercalated metaophiolitic and metasedimentary rocks and is characterized by a complex evolution including nappe stacking and crustal thickening, followed by postorogenic extension in the northern Aegean area (Jolivet and Brun, 2008, and references therein). Two main stacked units have been distinguished, the upper and lower, that are separated by the Nestos thrust fault (Fig. 1) (Ricou et al., 1998; Turpaud and Reischmann, 2009). The upper unit encompasses the Southern Rhodope Core Complex to the northeast and the north, and consists of orthogneisses, amphibolites, pelitic schists, and marbles. The orthogneisses correspond to plutonic protoliths of Permo-Carboniferous (270–291 Ma) and Late Jurassic-Early Cretaceous (134–164 Ma) ages (Liati, 2005; Turpaud and Reischmann, 2009, and references therein). The upper unit records high-pressure eclogite-granulite metamorphism dated at 140, 51, and 42 Ma (Liati, 2005), and ultrahigh-pressure metamorphism dated at 184 Ma (Mposkos and Kostopoulos, 2001; Liati, 2005; Perraki et al., 2006).

The present-day tectonic configuration of the Rhodope Massif is a result of Aegean-type postorogenic southwest-northeast extension and concurrent development of the Southern Rhodope Core Complex (see below) that constitutes essentially the lower unit (Dinter and Royden, 1993; Sokoutis et al., 1993; Bonev et al., 2006; Brun and Sokoutis, 2007). Aegean extension is controlled by large-displacement, low-angle detachment faults in the back arc of the Hellenic subduction zone (Bonev and Beccaletto, 2007; Brun and Sokoutis, 2007; Taymaz et al., 2007) and shares many points of similarity with the Basin and Range province of the western United States (e.g., Dinter, 1998; Brun and Sokutis, 2007). Extension in the northern Aegean started in the middle Eocene, driven by slab-rollback (Brun and Sokoutis, 2007; Brun and Faccenna, 2008), and culminated in the development of the Southern Rhodope Core Complex; it is characterized by very high heat flow values of as much as 2.5 HFU (100 mW/m$^2$), and geothermal gradients (avg 78°C/km). The final extensional stages were tied to orogenic collapse and marked by block faulting, Pliocene sedimentary basin formation, and extensive Oligocene-Miocene volcanism and associated hydrothermal ore mineralization (Marchev et al., 2005).

The Rhodope massif of northern Greece and southern Bulgaria hosts a range of metallic deposits: (1) carbonate replacement and skarn Pb-Zn(± Au ± Ag) mineralization (i.e., Madan and Thermes, Olympias, Madem Lakkos) (Kalogeropoulos et al., 1989, 1996; Nebel et al., 1991; Frei, 1995; Kilias et al., 1996; Kaiser-Rohrmeier et al., 2004; Marchev et al., 2005); (2) volcanic-hosted epithermal Pb-Zn-Cu(± Au-Ag) mineralization (i.e., Madjarovo); epithermal polymetallic (Ag, Te, Bi, Sn, Mo, base metals) and Au-Ag mineralization (i.e., Sappes, Perama Hill) (Shaw and Constantinides, 2001; Lescuyer et al., 2003; Voudouris et al., 2006; Rice et al., 2007), and porphyry Cu-Mo mineralization (Maronia)(Melfos et al., 2002); (3) sedimentary rock-hosted epithermal Au-Ag deposits (Ada Tepe, Surnak, Kuklitza prospects, Rosino, Stremtsi) (Marchev et al., 2005; Marton et al., 2007; 2010), and (4) nonsulfide Zn (Pb, Ag) ores (Thassos) (Boni and Large, 2003) (Fig. 1).

## The Southern Rhodope Core Complex

The Southern Rhodope Core Complex is the largest core complex in the Aegean region (Dinter and Royden, 1993; Sokoutis et al., 1993; Brun and Sokoutis, 2007). There are currently two models for its formation—one proposing exhumation along the "Strymon Valley fault zone" (Fig. 1), starting in the early to middle Miocene (Dinter and Royden, 1993; Dinter, 1998), and the other along the "Kerdylion detachment zone," starting in the middle Eocene (Brun and Sokoutis, 2007; Brun and Faccenna, 2008) (Fig. 1). It is beyond the scope of this paper to debate the merits of each model in detail and the reader is referred to the original texts. In terms of regional metallogenesis, the Kerdylion detachment model is preferred, as it allows a holistic metallogenic approach for mineralization in the Serbomacedonian-Rhodope metallogenic belt. Thus, unless otherwise noted, the following descriptions stem from Brun and Sokoutis (2007).

The Southern Rhodope Core Complex exhumed as a result of Aegean extension from middle Eocene to middle Mioocene. Exhumation was controlled by the Kerdylion detachment zone, and was accommodated by a 30° dextral rotation of the Chalkidiki peninsula that has been displaced for at least 120 km. The Kerdylion detachment zone corresponds to a west-southwest–dipping mylonitic shear zone consisting of migmatitic gneisses and granites, and separates the Kerdylion Massif in its footwall from the Serbomacedonian Massif of the Chalkidiki peninsula (Fig. 1); the Kerdylion Massif represents the upper brittle crust since the middle Eocene. The Southern Rhodope Core Complex displays some uncommon characteristics in relation to classical basin and Range Cordilleran core complexes. Within the entire complex, there is a regionally consistent extensional ductile fabric developed during exhumation, with a very uniform top-to-the-southwest sense of shear. The main foliation of the complex is flat-lying across the core complex width (100 km) and contains a northeast-southwest–stretching lineation and associated ductile-brittle shear fabrics (see also Bonev and Beccaletto, 2007, and references therein). It should be noted that after removal of 25° block rotation, the Kerdylion detachment zone displays the same top-to-the-southweset sense of shear as the rest of the complex. Lineated rocks are typically Permo-Carboniferous mylonitic orthogneisses (270–291 Ma; Liati, 2005; Turpaud and Reischmann, 2009), and lesser paragneisses. These are overlain by alternations of locally mylonitic marbles and mica schists, and schistose amphibolites, most likely derived from Mesozoic

sedimentary and volcanic cover sequences. The late Oligocene-early Miocene syntectonic granitoid plutons of Symvolon intrude the metamorphic rocks along the southern margin of the complex in the vicinity of Mount Pangeon (Fig. 1) (Kyriakopoulos et al., 1989). Late Miocene to Quaternary extensional basins (i.e., Drama, Serres, Strymon basins, Fig. 1) above the exhumed metamorphic and plutonic rocks were controlled by Pliocene to Pleistocene east-west to northeast-southwest, and northwest-southeast–trending steep normal faults and flat ramp-type extensional structures. Most rocks of the complex have undergone Tertiary high-temperature and medium-pressure (Barrovian) amphibolite facies metamorphism, locally culminating in partial melting, with migmatization principally represented in the Kerdylion Massif (Kalogeropoulos et al., 1989). Regional cooling below 500°C in early to middle Eocene and below 300°C in late Eocene to early Oligocene were associated with extensional deformation and exhumation (see Brun and Sokoutis, 2007, and references therein).

### Geology of the Asimotrypes Gold Mineralization

The Asimotrypes gold mineralization is hosted mostly by marbles of the Transitional unit (Fig 2; Chatzipanagis, 1991). The Transitional unit consists of rhythmically alternating layers of albite schists (20–25 m thick) and mica schists (5–15 m thick) and lenses or blocks of mylonitized, ribboned and foliated impure (cipoline) marbles (a few to 100 m thick) and actinolite-plagioclase amphibolites. The Transitional unit has a thickness of ~600 m that represents an early Miocene regional ductile shear zone (Dinter, 1998), within which lies the contact between the overlying Marble unit and the underlying Pangeon Gneiss unit (Fig. 2), which collectively make up Mount Pangeon. The Marble unit of ~500-m thickness is made up of thin-bedded laminated impure dolomitic (+ calcite) marbles, folded and boudinaged dolomitic marbles, and thick-bedded calcitic marbles. The Pangeon Gneiss unit displays a structural thickness of ~1,500 m and consists of plagioclase-rich orthogneisses and mica schists (Dinter, 1998). The Pangeon Gneiss unit gneisses possibly represent the Permo-Carboniferous plutonic and/or sedimentary Southern Rhodope core complex basement and the overlying Transitional unit the Mesozoic Tethyan sedimentary and volcanic cover; the age of the Marble unit is poorly constrained. The metamorphic sequence has been intruded by postcollisional and late syntectonic, high K calcalkaline metaluminous granitoids that form the core of Mount Pangeon. The granitoids occur as separate intrusive bodies known as the "Pangeon granitoids" (Messolakia, Podochori, Mesoropi, and Nikisiani bodies) and they belong to the same pluton that is coeval with the Symvolon pluton (Eleftheriadis and Koroneos, 2003); the latter was emplaced ~22 to 21 Ma (early Miocene) (Dinter, 1998; Eleftheriadis et al., 1999). In the Asimotrypes area, ductile extension has the same characteristics as the rest of the complex. Marbles, schists, and granitoids exhibit mylonite-type fabrics with consistent top-to-the-southwest sense of shear (Chatzipanagis, 1991; Dinter, 1998; Brun and Sokutis, 2007). All rocks have a strong extensional flat-lying foliation, in general parallel to lithological boundaries, and most often display a northeast-southwest–oriented stretching lineation.

The host rocks in the immediate area of Asimotrypes which belong to the Transitional unit are predominantly impure marbles intercalated with mica schists and lesser amphibolites (Figs. 3, 4). The marbles contain mainly ferroan calcite and dolomite in variable percentages, and quartz, muscovite, chlorite, kaolinite, dickite, hornblende, talc, and pyrite impurities which may range from 15 to 40 vol percent. The marbles have been subdivided into different types on the basis of the major mineral phases, microstructure, grain size, and color (e.g., impure calcitic marble, coarse-grained white calcitic marble, calcitic (dedolomite) marble


FIG. 4. Field photographs of Asimotrypes host rocks and mineralization. A. Sharp contact between irregular, siliceous, gold-bearing lenticular bodies of variable thickness (QB) hosted by shear foliated marble horizons (pa1). Note that the flat-lying foliation of the host marble is overprinted by northwest-oriented brittle steep normal faults and fractures (V) interpreted as hydrothermal feeder conduits (see text for discussion). Adit (left side of photograph) is ~1.5 m high. B. Typical host metasedimentary rocks consisting of a succession of subhorizontal foliated dolomitic marbles, and flat-lying mica schists parallel to the mylonitic foliation of the marbles (base of photograph). Younger brittle subvertical normal faults (V) crosscut the succession. Hammer for scale.

mylonite) (Varti-Matarangas and Eliopoulos, 2005). The main mass of the marbles that host the gold mineralization is a highly deformed, shear-layered calcitic (dedolomite) marble mylonite. These marbles may contain significant concentrations of accessory quartz, mica, chlorite, and pyrite, between 15 and 35 vol percent. Shear-layering is defined by alternating centimeter-to-decimeter–thick, coarse-grained layers with a grain fabric characterized by large calcite porphyroclasts surrounded by a fine-grained matrix of calcite and lesser quartz and muscovite mica, resembling a "core and mantle" structure (Fig. 5A, B) (e.g., Bestmann et al., 2000) with finer-grained layers that consist of alternating ribbons of chlorite and muscovite mica with ribbons of microshear zones of calcite and quartz (Fig. 5C, D). Dedolomitization (or dolomite calcitization) (see Nader et al., 2008, and references therein) is expressed as large subhedral to euhedral (a few hundred μm in length) rhomb-shaped saddle dedolomite crystals (Fig. 5B), which may contain 6 to 9 mole percent $MgCO_3$, as well as relic ghost grains that have been revealed by staining (see Materials and Methods).

## Styles of Gold-Bearing Sulfide Mineralization and Alteration

The Asimotrypes mineralization is basically a disseminated gold-bearing arsenopyrite and, to a lesser extent, pyrite mineralization in impure mylonitic marbles. Arsenopyrite and pyrite mineralization are localized by a combination of structural and lithologic controls (Baker et al., 1993). The northeastern part of the Mount Pangeon, including Asimotrypes, displays a 2,000-m vertical section from the base of Mount Pangeon and the Nikisiani granite up through Asimotrypes to the top that exhibits two mineralogically similar and spatially coincident mineralization styles with a supergene overprint: (1) strata-bound replacement of the Transitional unit marbles; this is the main style and referred to as replacement-type mineralization in the following text, and, lesser (2) quartz-sulfide lenses, and sulfide disseminations, within discordant subvertical brittle normal faults and joints that crosscut all rock types of the Transitional and Marble units, including the granitoids; these are referred to here as vein-type mineralization, or "veins."

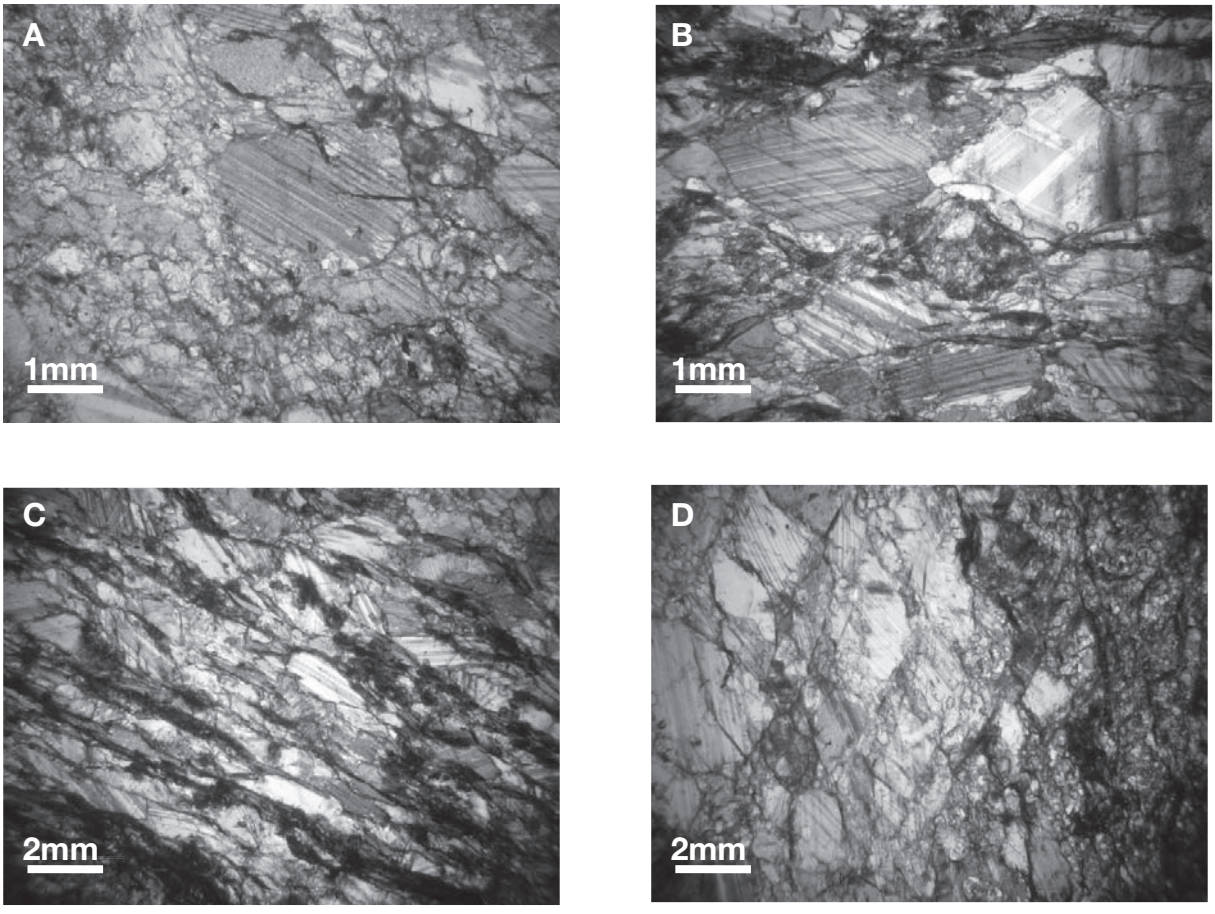


FIG. 5. Photomicrographs of typical foliated host marble mylonite microstructures showing compositional and grain size layering. A and B. "Core and mantle"-like structure, denoting ductile behavior. Coarse-grained, fish-shaped, rhombohedral or anhedral twinned calcite (dedolomite) porphyroclasts are surrounded by a microcrystalline to fissile matrix of calcite, quartz, chlorite, and muscovite; note the higher percentage of phyllosilicate phases in B. Large calcite (dedolomite) porphyroclasts show deformation twins with offset. C. Ribbon-like structure. Microlayering is defined by alternating ribbons of fine-grained chlorite and muscovite with ribbons of coarser-grained sheared calcite and quartz. D. Sharp contact between coarse-grained "core and mantle" and fine-grained ribboned layers. Foliation is defined by the preferential orientation of phyllosilicates.

*Replacement-type mineralization*

This style is concentrated at, and controlled by, the intersections of several mylonitic and hydrothermally altered marble horizons of the Transitional unit, with northwest-southeast– to east-west–trending, steeply dipping quartz veins which fill high-angle brittle normal faults and fractures that seem to have focused fluid flow during gold mineralization. In particular, this mineralization is developed along the lithological boundary between intercalated overlying mica schists, which represent a less permeable cap rock, and the more permeable sheared marbles, and within the marble. These mineralized zones individually measure a thickness of as much as 3 m and show flat-lying shear sense with top-to-the-southwest displacement tunable to the regional northeast-southwest–directed extension that characterizes the entire complex; dip is ~30° to the east. Replacement-type mineralization extends more than 2,000 m along strike and fills the total ~600-m stratigraphic interval of the Transitional unit (Fig. 3). Replacement bodies form as elongate, discontinuous, tabular, lenticular or irregular shapes (1–2 m wide, ~1 m thick, and ~5 m long (see Fig. 4A). Gold-bearing siliceous bodies are clearly distinguished and postdate earlier boudinaged and isoclinally folded quartz that occurs within the mica schist. Also, there is no calc-silicate skarn development in association with the mineralized zones at Asimotrypes.

*Hydrothermal alteration:* The most apparent hydrothermal alteration related to replacement-type mineralization includes silicification, carbonate dissolution, decarbonation, and sulfidation of the host marbles. The intensity of silicification varies within the mineralized zone from partial to complete quartz replacement of marble (Fig. 6A, B). Complete pervasive silicification typically produced small siliceous bodies (within the larger areas of altered marble), with less than 1.5 percent carbonate content, which host most of the gold. Microscopic calcite (dedolomite) relics occur locally (Fig. 6C). Silicification is also shown by fine drusy quartz lining carbonate dissolution-related vugs (Fig. 6F). Silicification and deposition of quartz also occur along the high-angle brittle normal faults and are manifested by the presence of vein-type mineralization (see below). Gold-bearing siliceous replacement bodies are associated with and occur as a discordant wide halo adjacent to the centrally located northwest-southeast– to east-west–trending, high-angle, brittle faults and fractures (Fig. 3). Sulfidation occurs in the form of disseminated arsenopyrite, pyrite, and As pyrite that are ubiquitously present in these siliceous rocks (Fig. 6D-F); the amount of sulfide can vary widely, but may be as much as 35 vol percent of the mineralized rocks. Arsenopyrite constitutes >90 percent of the total sulfide content of the gold-bearing siliceous bodies. Decarbonation of marble is evident from small anhedral carbonate relics within hydrothermal jasperoidal quartz (see below) and gold-bearing arsenopyrite (Figs. 6C, 7E). Dissolution of marble is also shown by fine drusy quartz lining vugs (Fig. 6F). In highly silicified rocks, primary mylonitic textures are largely destroyed; these commonly grade into silicified marble that retains its original mylonitic texture within a few-centimeter-thick alteration envelope. These hydrothermal envelopes are enriched in base and precious metals, i.e., Au, Ag, Pb, Zn, As, and S and $SiO_2$ (see below and App.). Hydrothermally altered interbedded mica schists and amphibolites consist of quartz, chlorite, phlogopite, sericite, and clinozoisite, and chlorite, quartz, and pyrite overprinted by marcasite-pyrrhotite ± titanite ± leucoxene, respectively; the former may contain 20 to 440 ppb gold (App.).

*Vein-type mineralization or "veins"*

This style refers essentially to small, semimassive quartz-sulfide lenticular pods, veinlets, and breccias with disseminated sulfide minerals that occur along northwest-southeast– to east-west–trending high-angle brittle faults and fractures, which strike perpendicular to the flat-lying ductile, shear foliation of the host rocks, dip steeply to the southwest, and reflect structural control of mineralization (Fig. 3). The pods are generally narrow, varying from 2 to 5 cm in diameter, with horizontal extensions of about 500 m within the Transitional unit, and they can be traced for 2,000 m along strike to the top of Mount Pangeon. Vein-type mineralization is best developed in the hanging wall to the mineralized shears adjacent to their intersections with the faults and fractures; here, crackle and mosaic marble breccias dipping 55° to the north are common, and are characterized by extensive replacement of the sulfide minerals by supergene oxides (see below). Moreover, "vein" mineral assemblages change with host rock. In granite, pyrite + quartz to pyrite + quartz + sericite and/or quartz + sericite assemblages are the main hydrothermal minerals. Arsenopyrite + pyrite + quartz (+ limonite) to pyrite + chalcopyrite + quartz (+ chrysocolla, limonite) dominate where the faults and fractures cross marble and mica schist units at higher topographic levels (Fig. 3). Vein-type mineralization is characterized by the same type of hypogene sulfide and supergene oxide mineralogy that accompanies the replacement type. These structural, mineralogical, and stratigraphic relationships, combined with geochemical data (see below) suggest that these northwest-southeast and east-west–oriented faults and fractures represent the principal metalliferous fluid conduits that promoted fluid migration by enhancement of fracture permeability in the mineralized zones. Moreover, these northwest-oriented, high-angle normal faults hosting vein-type mineralization have been interpreted as an expression of synextensional or late extensional rolling hinge-type deformation synchronous to exhumation of the Southern Rhodope Core Complex; these structures are coeval with post-Tortonian northwest-oriented regional brittle normal faulting that overprints both core complex metamorphic rocks and the Messolakia granitoid, and that controls Neogene sedimentary basins such as Strymon, Serres, and Drama (Fig. 1) (Dinter, 1998; Tranos et al., 2008; Tranos, 2011). The distribution of gold mineralization appears to be related the geometry of these brittle structures.

*Supergene gold mineralization*

Supergene oxidation of sulfide minerals has produced abundant colloidal Fe and Mn oxides and hydroxides (limonite) that occur as boxworks, bands, veins, impregnations, thin crusts, and/or stains. Limonite is best developed within crackle and mosaic marble breccias at and adjacent to the intersections of mineralized shears with the quartz veins, as well as in the form of ~2- to 5-cm-wide envelopes of the sulfidized marble.

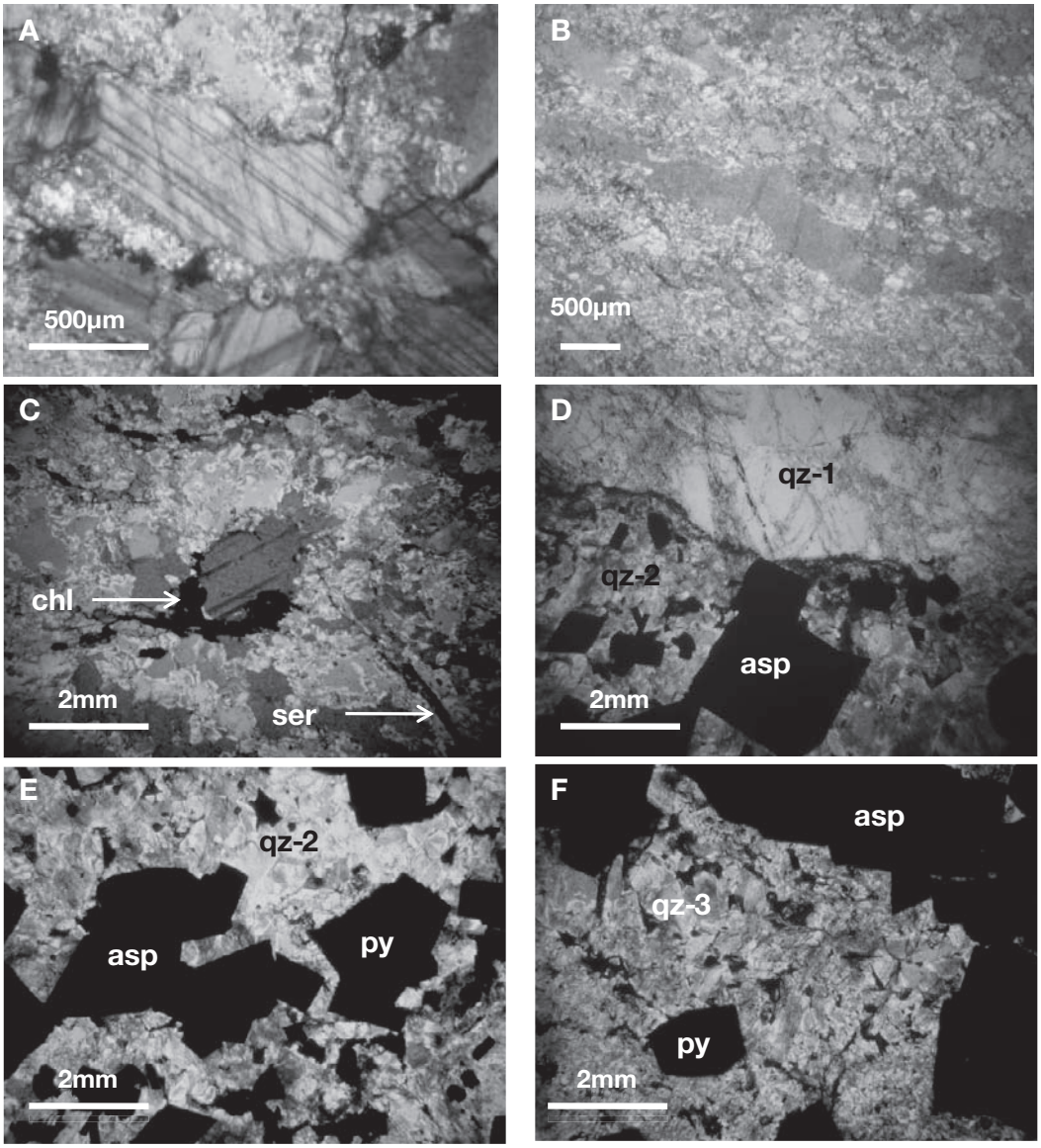


FIG. 6. Microphotographs of variably altered and mineralized siliceous rocks from Asimotrypes. A. Partially silicified marble mylonite. B. Barren coarse- to medium-grained banded quartz-1. The textural features of quartz-1reflect the texture and grain size of the replaced marble mylonite. C. Reticulate or xenomorphic texture of jasperoidal quartz-2, with variable grain size enclosing calcite relics and chlorite, suggests formation by pervasive replacement of calcitic marble; sericite (ser) and chlorite (chl) constitute hydrothermal alteration minerals. D. Distinctive banded quartz-1 (qz 1) is overgrown by quartz-2 (qz 2); Au-sulfide minerals (dark rhombs and cubes) are consistently enclosed within quartz-2 crystals. E. Typical fine-grained gold mineralized jasperoidal quartz-2 with enclosed auriferous arsenopyrite (rhombs, asp) and pyrite (cubes, py). F. Coarse drusy quartz-3 (qz 3) filling vugs and larger open spaces interstitial to intergrown gold-bearing arsenopyrite (asp), pyrite (py), and quartz-2.

### Mineralogy and Mineral Chemistry

The auriferous siliceous body gangue is composed mainly of quartz characterized by three textural varieties that represent an equal number of stages of hydrothermal silicification and mineralization development: banded quartz (quartz-1), jasperoidal quartz (quartz-2) that is the main host of the gold-bearing sulfide minerals, and rare, late-stage drusy quartz (quartz-3). Banded quartz preserves original mylonitic features; it represents fine- to medium-grained quartz replacements of calcite (dedolomite) with core and mantle- and/or ribbon-like texture and contains only traces of sulfide minerals (Fig. 6A, B). Deformation microtextures in quartz are also expressed as intragranular and transgranular healed fractures in quartz grains with deformation lamellae, undulose extinction, and sutured grain boundaries. Original quartz is difficult to distinguish from hydrothermal quartz. Quartz-1 occurs as random, narrow, discontinuous zones that run parallel to the shear foliation. It is mainly developed at the periphery of the auriferous siliceous bodies and marks the transition from weakly silicified marble, which retains its original texture, to dominantly jasperoidal quartz-2 with complete obliteration of original shear features. Jasperoidal quartz-2 overgrows

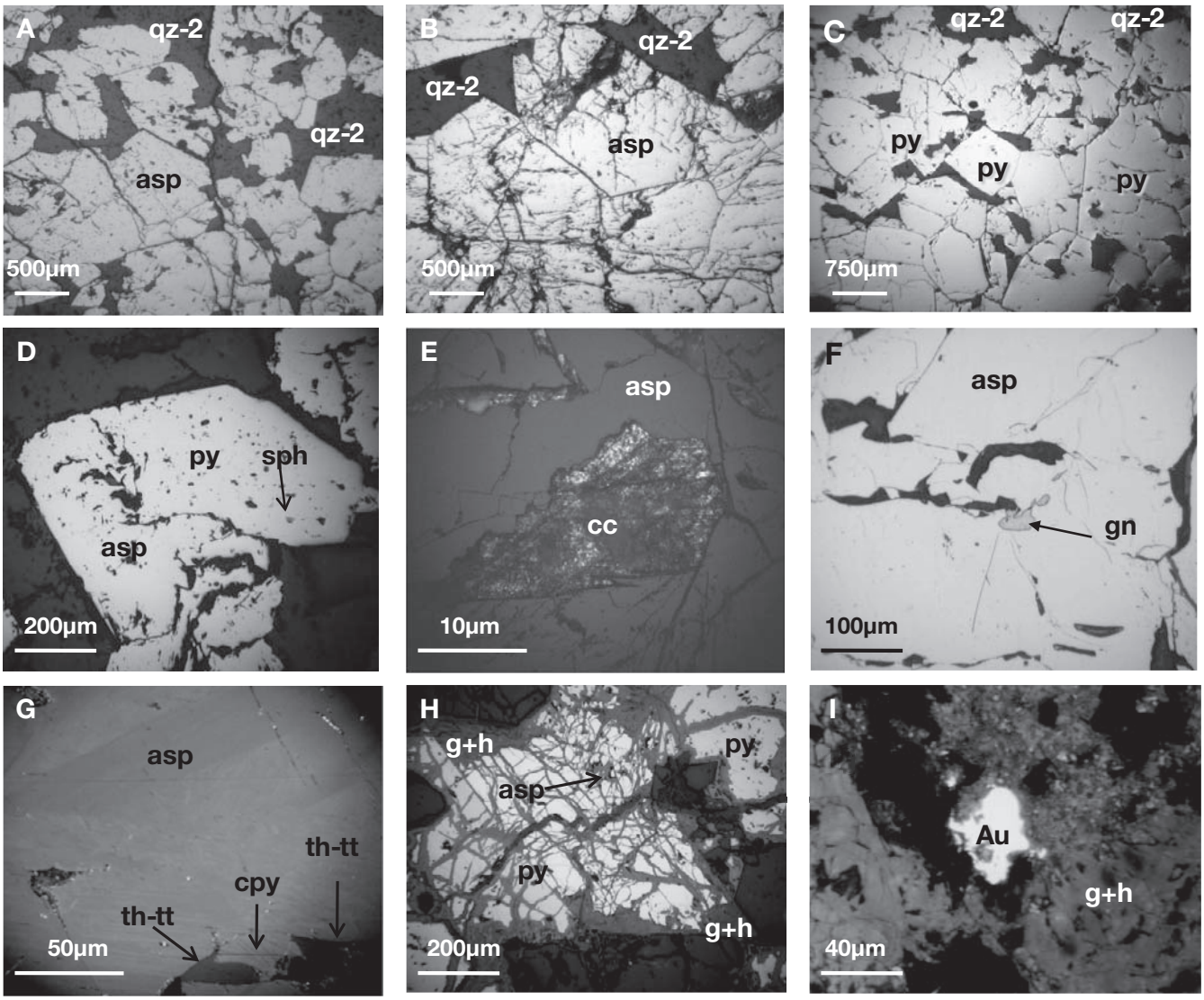


FIG. 7. Reflected light photomicrographs of textural relationships between minerals of the paragenetic assemblages in the Asimotrypes gold mineralization. A. B. Typical monomineralic aggregates of gold-bearing arsenopyrite grains set in a matrix of jasperoidal quartz-2 (dark). Much of the arsenopyrite displays euhedral to subhedral crystal shapes; hairline brittle microfractures or irregularly embayed textures are present (B). Arsenopyrite shows a porous texture and contains xenomorphic inclusions of quartz, carbonate, and other sulfide minerals (see below). C. D. Typical occurrence of arsenopyrite and pyrite aggregate inbedded in jasperoidal quartz-2 (dark). Associations between arsenopyrite and pyrite imply cocrystallization, although in places, arsenopyrite encloses and has possibly corroded pyrite (D) (arsenopyrite grains are not marked by abbreviations in C). Note porous texture in pyrite and silicate, carbonate and sphalerite inclusions. E. Large twinned calcite inclusion within porous arsenopyrite. F. G. Arsenopyrite crystals with coeval inclusions of galena, chalcopyrite, and tetrahedrite-tennantite (G). Note complex growth twinning or zoning in host arsenopyrite. H. Sieve-texture of supergene goethite + hematite in fractures overprinting arsenopyrite and pyrite. I. Large gold grain in supergene ferruginous (hematite + goethite) matrix. Mineral abbreviations: cc = calcite, cpy = chalcopyrite, py = pyrite (including arsenian pyrite), qz = quartz, asp = arsenopyrite, th-tt = tetrahedrite-tennantite, gn = galena, sph = sphalerite, g+h = geothite+hematite, Au = gold.

quartz-1 and is characterized by a crystalline mosaic, saccharoidal, or xenomorphic texture, with variable grain sizes ranging from ~5 to 300 $\mu$m; the latter contains rare fine- to medium-grained anhedral grains of calcite (Fig. 6C), which are interpreted to represent relicts of the host rock. Quartz-2 is locally decorated by fluid inclusion trails along transgranular, healed brittle microfractures which also transect coexisting auriferous sulfide minerals. Hydrothermal phyllosilicate phases may accompany quartz–2 (Fig. 6C). Rarely, fine drusy quartz (quartz-3) is found lining carbonate dissolution-related vugs (Fig. 6F). In some samples, all three stages of silicification can be present.

The gold-bearing assemblage of hypogene mineralization consists of arsenopyrite and arsenian pyrite dispersed within jasperoidal quartz-2 (Fig. 6D-F). Gold was found at submicroscopic amounts in arsenopyrite and arsenian pyrite, and as visible native free gold associated with supergene Fe minerals. Gold-bearing arsenopyrite occurs as aggregate masses

consisting of interlocking medium- to coarse-grained idiomorphic to subidiomorphic grains, in the size range of 1.5 mm to less than 100 $\mu$m, which are present in a rhombic, triangular, or acicular form (Fig. 7A-C). Arsenopyrite is also intergrown with arsenian pyrite and pyrite; these sulfide minerals commonly have straight, sharp, and crystal-shaped or mutually interpenetrating grain boundaries, and both are consistently associated with massive jasperoidal quartz-2, indicating that they were deposited within one evolving hydrothermal event and were essentially coeval (Fig. 7C, D). Gold-bearing sulfide minerals have a porous texture (Fig. 7A, D), and rare carbonate inclusions within pores, indicating that they are marble replacement products (Fig. 7E) (Putnis, 2009). However, cataclastic or irregularly embayed textures of these sulfide minerals are common (Fig. 7B, D), indicating a syndeformation timing of deposition, and that the mineralizing system was subject to brittle deformation as it developed. Galena, tetrahedrite-tennantite, and chalcopyrite occur as inclusions in euhedral arsenopyrite (Fig. 7F, G). Supergene overprint includes colloidal Fe oxides and hydroxides in the form of goethite + hematite containing native gold grains ranging from 20 to 40 $\mu$m in diameter (Fig. 7H, I), and lesser covellite, malachite, cerrussite, and chrysocolla. An interpreted paragenetic sequence within the main mineralized area is shown in Figure 8.

Figure 9A and B shows reflected light microphotographs of gold-bearing arsenopyrite with complex crystallographic zoning patterns that may represent growth twinning (Kretchmar and Scott, 1976; Pracejus, 2008) and/or chemical growth zoning (e.g., Benzaazoua et al., 2007, and references therein). The backscattered electron (BSE) imaging technique failed to reproduce these complex patterns, signifying small differences of average atomic number across the arsenopyrite crystals. However, BSE images reveal that gold-bearing arsenopyrite grains have irregular, intragranular compositional zones on a scale of <10 $\mu$m, observed between darker and brighter domains on BSE images (see Fig. 9C-E). The compositional zoning is related to variations in As/S ratio, and it is expressed as an increase in As atomic number from 29.4 to 32.5 at. percent, correlating with a decrease in the S content from 38.02 to 35.4 at. percent.

Electron microprobe analyses (EMPA) show that arsenic in arsenopyrite ranged from 41.7 to 43 wt percent (mean = 42.5 wt %). Figure 10A and Table 1 present 50 gold secondary ion mass spectrometry (SIMS) analyses of gold-bearing arsenopyrite and arsenian pyrite grains. SIMS analyses show that gold in arsenopyrite and arsenian pyrite range from 0.5 to 29 ppm (mean = 11.6 ppm), and 0.14 to 11 ppm (mean = 2.3 ppm), respectively (Table 1); arsenic ranged from 0.01 to 3.8 wt percent (mean = 1.35 wt %) in arsenian pyrite. Figure 10B documents the positive correlation between arsenic and gold in SIMS analyses of arsenian pyrite, as is commonly the case for invisible gold-bearing arsenian pyrites elsewhere (e.g., Cook and Chryssoulis, 1990; Hofstra and Cline, 2000; Cline, 2001). Moreover, Figure 10A shows that gold is preferentially concentrated in arsenopyrite compared to arsenian pyrite. Element-specific mapping obtained by SIMS (Fig. 11) shows that gold exhibits a primary inhomogeneous distribution pattern that appears to mimic finely banded, growth-twinning lamellae or growth zones(see Fig. 9A, B); in addition, gold is always accompanied by arsenic, but not vice versa. With the presently available data, it is not possible to determine whether gold in arsenopyrite is structurally bound or occurs as submicroscopic inclusions (<1,000 Å) of free gold. Collectively, the reflected light, BSE, and SIMS data provide evidence that invisible gold in arsenopyrite is crystallographically controlled and is associated with growth phases of arsenopyrite.

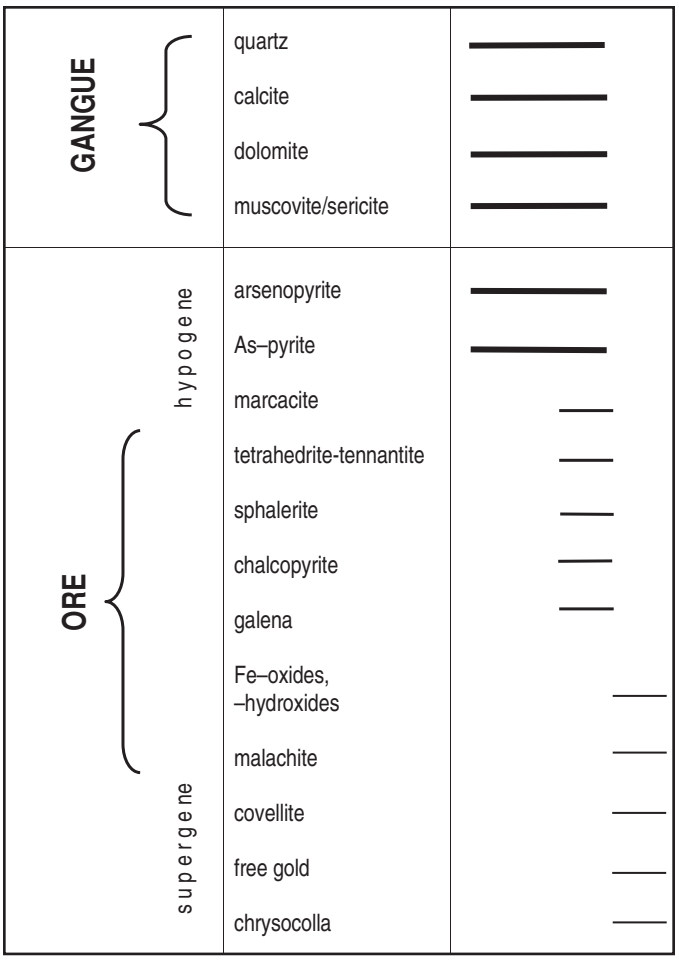


FIG. 8. Generalized paragenetic sequence of the Asimotrypes mineralization.

### Geochemistry of Gold Mineralized Zones

Geochemical data of representative variably mineralized rocks are provided in the Appendix.

The mineralized zones are defined by gold concentration values and overall abundance of sulfide minerals. The gold concentration in samples from replacement-type mineralization ranges between 3.2 and 16.60 ppm (mean = 6.5 ppm) (App.); the highest gold grades occur close to the intersection with the crosscutting quartz veins, and drop off toward the margins of the siliceous bodies (App.). Most gold-bearing samples in replacement-type mineralization contain less than 1.5 wt percent CaO (App.). Where dissolution and silicification of marble were not accompanied by deposition of sulfide minerals, gold grades are less than 150 ppb (App.–MWR). The center of the siliceous lenses or pods in the Transitional unit contains the highest (as high as 16.6 ppm) concentrations

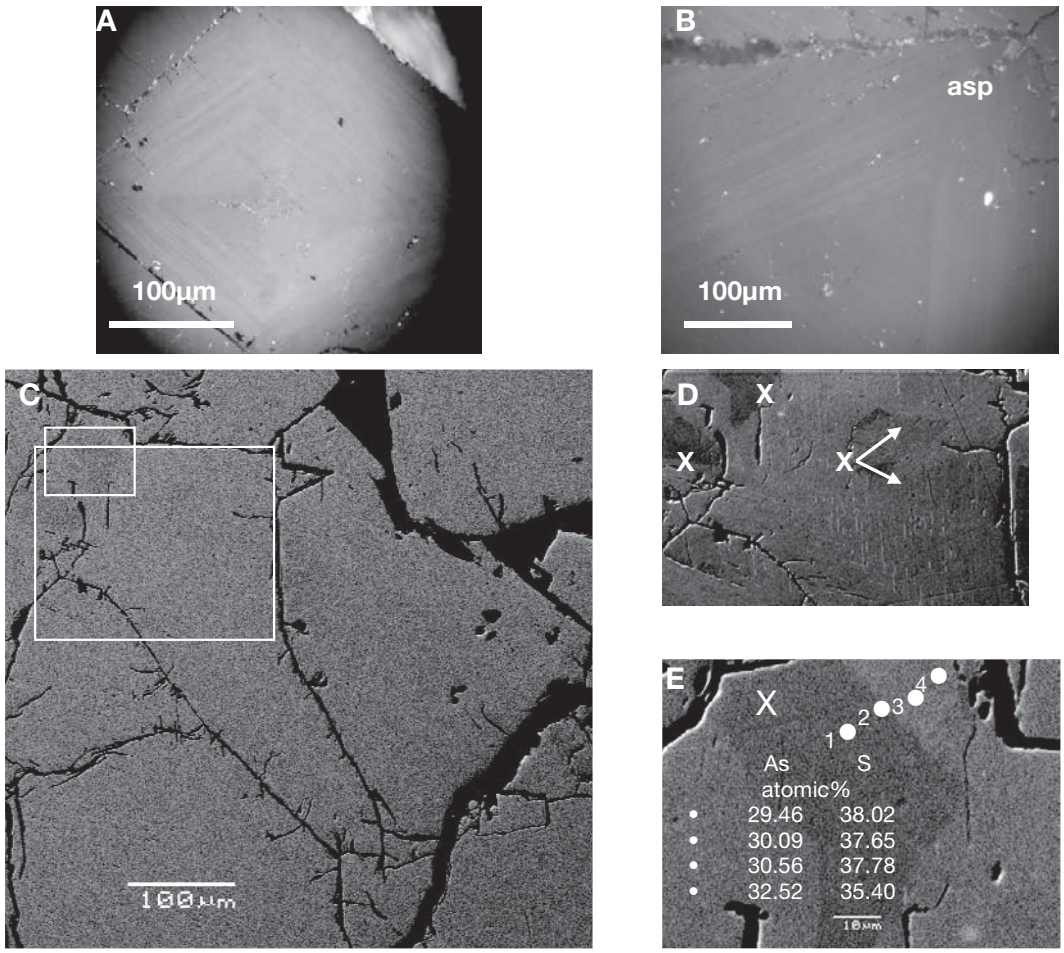


FIG. 9. A. B. Euhedral arsenopyrite crystals showing at least two sets of superimposed and crosscutting linear bands or lamellae, running obliquely to crystal faces, possibly representing polysynthetic growth twinning ("sand-glass" twinning of arsenopyrite according to Pracejus (2008)(A), or growth oscillatory zoning crosscut by a secondary diffusion zoning (B)(Benzaazoua et al., 2007). C.D.E. Collection of backscattered electron (BSE) images defining the characteristics of within-grain irregular compositional zoning on arsenopyrite. C. Aggregate of anhedral arsenopyrite grains. D. Close-up of C, with contrast adjusted to show darker rectangular to irregular domains marked with an X, which may belong to crystallographic zones; these domains reflect lower As and higher S content compared to brighter areas; 29.46–30.09 As at. percent in darker domains, and 30.56–32.52 at. percent in brighter domains (electron microprobe analyses are shown in E). Note internal linear fabric in D.

of gold with an average value of 6.5 ppm, whereas margins may contain 1 to 3 ppm gold. Sulfide lenses along the northwest-southeast fractures within the Transitional unit are also enriched in gold (as much as 13.5 ppm; avg = 6.7 ppm) (Fig. 3).

Chemical analyses of supergene limonites have shown gold contents up to 6.7 ppm (App.–LRM); the form of this gold is unknown.

Gold grades and the abundance of sulfide minerals decrease rapidly when the veins cross Marble unit marble and granite above and below the Transitional unit (App.; Fig. 3). Gold distribution shows a consistent variation from the Nikisiani Granitoid through the Transitional to the Marble units and the top of Mount Pangeon, a vertical distance of 1,000 m.

The average (max) assays from 16 unoxidized auriferous samples from the mineralization containing >0.5 ppm gold (App.) are 7 ppm Au (16.6), 47 ppm Ag (320), 25,000 ppm As (45%), 54 ppm Sb (100), 53.4 ppm Bi (107), 4.6 ppm Te (33), 3.6 ppm Se (5), and 0.6 (8) wt percent Pb, 0.2 (1.7) wt percent Zn, and 1.9 (16.3) wt percent Cu. Gold/silver ratios are 1 to 2 (see App.) and Au correlates very well with As ($r^2 = 0.75$), reflecting the Au-arsenopyrite association, and there are good correlations with Sb ($r^2 = 0.6$), Bi ($r^2 = 0.6$), and Ag ($r^2 = 0.5$). Silver strongly correlates with Cu ($r^2 = 0.84$) and Cr ($r^2 = 0.71$), for reasons that are not clear. Copper, lead, zinc, arsenic, silver, and antimony show poor interelement correlation ($r^2 < 0.4$). The average concentrations of As, and Cu, Pb, and Zn reflect the predominance of arsenopyrite, with minor chalcopyrite, galena, and sphalerite in the mineralized bodies.

This gold grade distribution, combined with the inferred geologic contemporaneity of shear zones and crosscutting quartz-veins within the extensional deformation framework of the core complex, supports the interpretation of the northwest-southeast– to east-west–trending, steeply dipping veins as principal local conduits for hydrothermal fluids during sulfide and gold mineralization. However, the bulk amount of gold was deposited away from these structures within favorable stratigraphic units (i.e., marble).

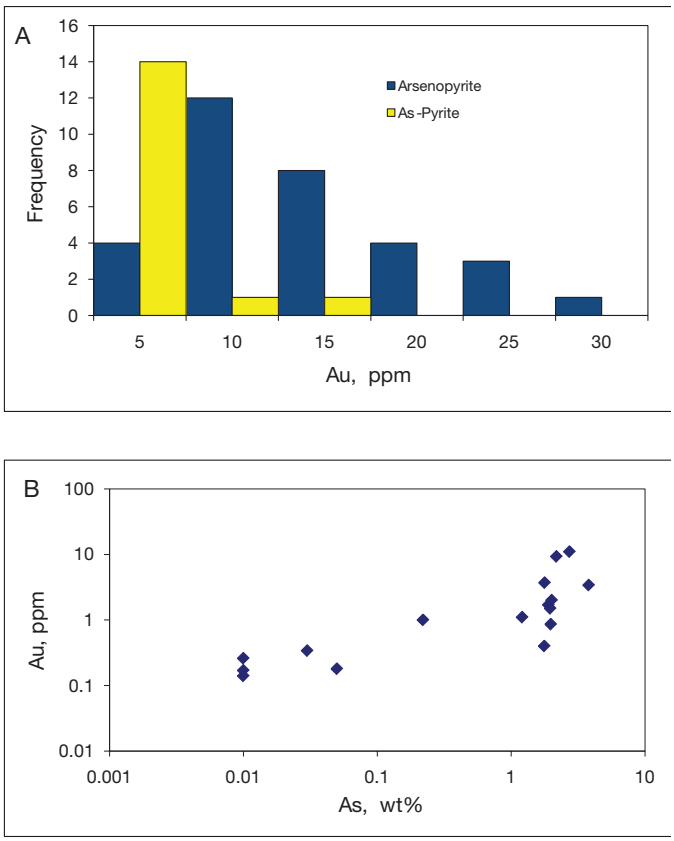


FIG. 10. Secondary ion mass spectrometry (SIMS) data from Asimotrypes. A. Histograms showing gold contents for arsenopyrite and arsenian pyrite; enrichment of gold in arsenopyrite relative to arsenian pyrite is shown. B. Distribution of gold versus arsenic for SIMS analyses of arsenian pyrite.

TABLE 1. SIMS Analyses for As and Au of Arsenian Pyrite and Arsenopyrite

| Sample and grain no. | Phase | As (wt%) | Au (ppm) |
|---|---|---|---|
| NIG14–3 | As–py | 1.9 | 1.7 |
| NIG14–4 | As–py | 0.01 | 0.26 |
| NIG14–8 | As–py | 3.8 | 3.4 |
| NIG14–11 | As–py | 2.01 | 2.01 |
| NIG14–14 | As–py | 0.03 | 0.34 |
| NIG14–15 | As–py | 1.78 | 3.7 |
| NIG14–24 | As–py | 1.77 | 0.4 |
| NIG14–26 | As–py | 1.98 | 0.86 |
| NIG14–27 | As–py | 0.05 | 0.18 |
| NIG14–29 | As–py | 1.96 | 1.5 |
| NIG14–30 | As–py | 2.18 | 9.3 |
| NIG14–33 | As–py | 1.21 | 1.1 |
| NIG14–34 | As–py | 0.22 | 1.01 |
| NIG14–36 | As–py | 0.01 | 0.17 |
| NIG14–37 | As–py | 2.73 | 11 |
| NIG14–42 | As–py | 0.01 | 0.14 |
| NIG14–1 | Aspy | | 2.5 |
| NIG14–2 | Aspy | | 16 |
| NIG14–5 | Aspy | | 9.5 |
| NIG14–6 | Aspy | | 7.01 |
| NIG14–7 | Aspy | | 10 |
| NIG14–9 | Aspy | | 14 |
| NIG14–10 | Aspy | | 11 |
| NIG14–12 | Aspy | | 16 |
| NIG14–13 | Aspy | | 9.3 |
| NIG14–16 | Aspy | | 14 |
| NIG14–17 | Aspy | | 9.6 |
| NIG14–18 | Aspy | | 6 |
| NIG14–19 | Aspy | | 29 |
| NIG14–20 | Aspy | | 6 |
| NIG14–21 | Aspy | | 2.9 |
| NIG14–22 | Aspy | | 6.6 |
| NIG14–23 | Aspy | | 24 |
| NIG14–25 | Aspy | | 24 |
| NIG14–28 | Aspy | | 0.47 |
| NIG14–31 | Aspy | | 22 |
| NIG14–32 | Aspy | | 6.8 |
| NIG14–35 | Aspy | | 19 |
| NIG14–38 | Aspy | | 4.6 |
| NIG14–39 | Aspy | | 14 |
| NIG14–40 | Aspy | | 15 |
| NIG14–41 | Aspy | | 9.2 |
| NIG14–43 | Aspy | | 13 |
| NIG14–44 | Aspy | | 9.8 |
| NIG14–45 | Aspy | | 6.1 |
| NIG14–46 | Aspy | | 20 |
| NIG14–47 | Aspy | | 15 |
| NIG14–48 | Aspy | | 14 |
| NIG31–1 | Aspy | | 7.9 |
| NIG31–2 | Aspy | | 4.7 |

As–py = arsenian pyrite, Aspy = arsenopyrite

## Fluid Inclusions

### *Occurrence and timing of the fluid inclusions with respect to quartz formation and their relationship to gold mineralization*

Samples of replacement-type gold mineralization bodies and vein-type mineralization, found close to their intersection with replacement type, contain primary, pseudosecondary, and secondary fluid inclusions. Undisputable primary fluid inclusions occur only within jasperoidal gold-bearing quartz-2 and quartz-3. These inclusions occur in the following ways: (1) in clusters in the middle of crystals, (2) along planes that mark growth zones, (3) as individual isolated inclusions or in random three-dimensional patterns throughout a single grain (Fig. 12A, E). Typically, the fluid inclusions are irregular to ovoid in shape and the size of fluid inclusions ranges from <5 to 35 $\mu$m. Pseudosecondary fluid inclusions are very common in quartz-2. These fluid inclusions are present as discontinuous trails that mark healed fractures within individual grains that do not crosscut the grain boundary (Fig. 12B). The orientation of trails in individual quartz grains is variable and interpreted to be related to fractures that formed during extension and exhumation (Fig. 12B). The individual fluid inclusions within these trails are similar in appearance and shape to primary fluid inclusions, and are generally <40 $\mu$m in maximum dimension. Secondary fluid inclusions commonly define trails that crosscut quartz boundaries. These inclusions clearly postdate the entrapment of primary and pseudosecondary inclusions. The fluid inclusions in these trails are usually small (<10 $\mu$m), mostly equant, and are usually elongated in the direction of the trail (Fig. 12C). Secondary fluid inclusions occur also in the form of naturally decrepitated and/or leaked inclusions which occur in random clusters within quartz or around the grain boundaries (Fig. 12D).

Primary and/or pseudosecondary inclusions are intimately related to gold-bearing sulfide minerals and are interpreted to have trapped the gold-bearing fluids (Fig. 12A, B). Trail-bound secondary inclusions are interpreted to postdate gold-bearing sulfide precipitation.

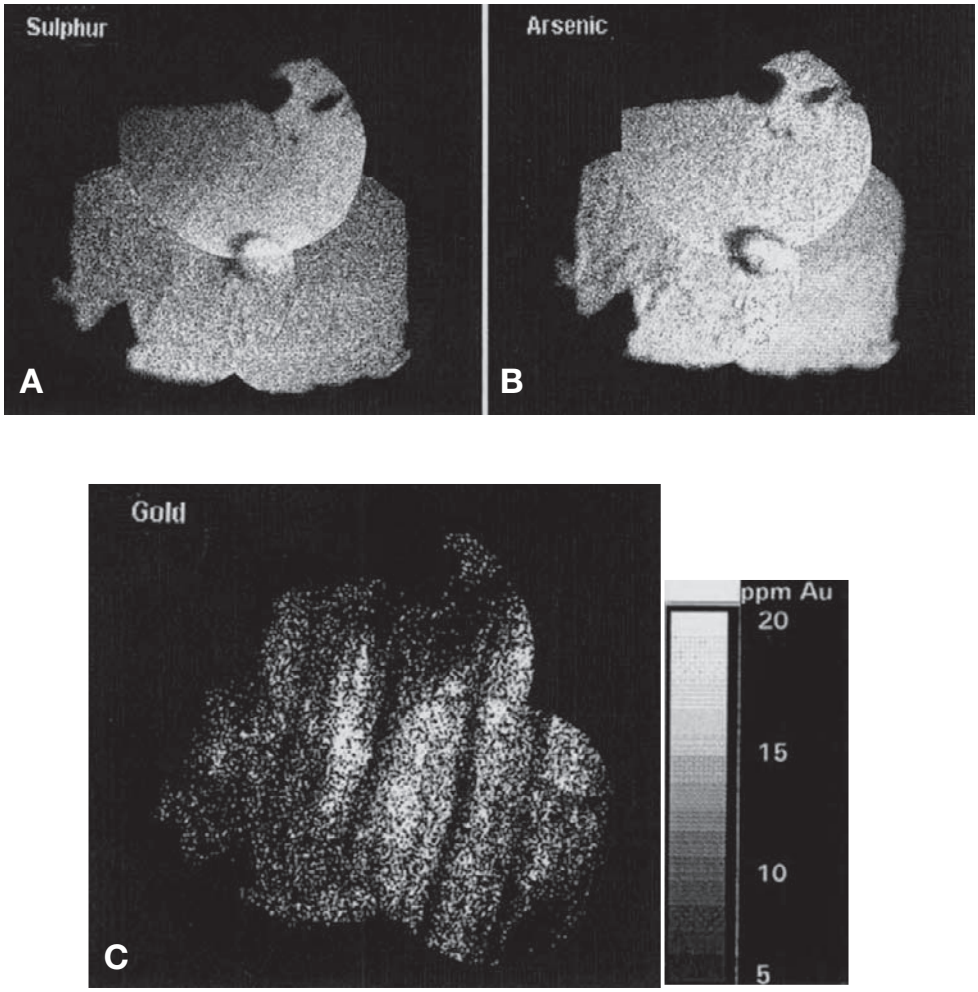


FIG. 11. SIMS mass-specific maps showing distribution of sulfur (mass 34), arsenic (mass 75), and gold (mass 197) in arsenopyrite from Asimotrypes. A. SIMS map for sulfur. B. SIMS map for arsenic. C. SIMS image of gold distribution. Gold is distributed inhomogeneously along crystallographic zones. Zones of fine banding are discernible. The dark gray scale gives the range of gold content in ppm. Light areas represent elevated concentrations of the respective element.

*Types of fluid inclusions*

Four types of fluid inclusions in varying abundance have been distinguished on the basis of inferred bulk composition and origin: (I) $CO_2$-rich inclusions, (II) mixed $H_2O$-$CO_2$ inclusions, (III) aqueous inclusions, and (IV) naturally decrepitated/leaked inclusions.

*Type I:* $CO_2$-rich inclusions are primary or pseudosecondary and consist of a single liquid or two phases (liquid $CO_2$ + vapor $CO_2$) at room temperature and they do not form a gas hydrate on cooling to temperatures below –40°C. Dark transparent edges along the inclusion walls indicate a minor (<10 vol %) liquid water phase (Fig. 12E, F). Type I inclusions are relatively rare, making up less than 10 percent of all inclusions; they are mostly equant, often with negative crystal shapes, and are always associated with other types of inclusions (Fig. 12E, F). Inclusions that are evaluated to contain 90 vol percent or more carbonic phase are classified as type I $CO_2$-rich inclusions.

*Type II:* $H_2O$-$CO_2$ inclusions are primary or pseudosecondary and contain an undersaturated aqueous liquid phase and a two-phase bubble of liquid + vapor $CO_2$ at room temperature. They are the most abundant type, are characterized by regular to irregular shapes, and generally range between 5 and 35 $\mu$m in size (Fig. 12E, F). Groups of type II inclusions exhibit a large variance, from 10 up to 80 percent, in the volumetric percentage of the carbonic phase and classically have $CO_2$-rich type I inclusions associated with them. Primary or pseudosecondary type II (and I) inclusions represent more than 90 vol percent of all inclusions present in gold-mineralized samples. Commonly, type II aqueous carbonic inclusions in euhedral quartz-2 are spatially related to gold-bearing Fe sulfide minerals (Fig. 12A, B), and are interpreted to have trapped the gold-bearing fluid at Asimotrypes.

*Type III:* These are aqueous two-phase inclusions, characterized by a vapor bubble in an aqueous liquid at room temperature. Their shapes vary from angular to subrounded, or rounded to ellipsoidal, and vapor proportions are of about 10 to 40 vol percent. Sizes rarely exceed 15 $\mu$m in diameter, ranging from <5 to 30 $\mu$m. Clathrate melting was observed in some type III inclusions and that melting is indicative of traces of $CO_2$ in the gas phase. Some inclusions of this type

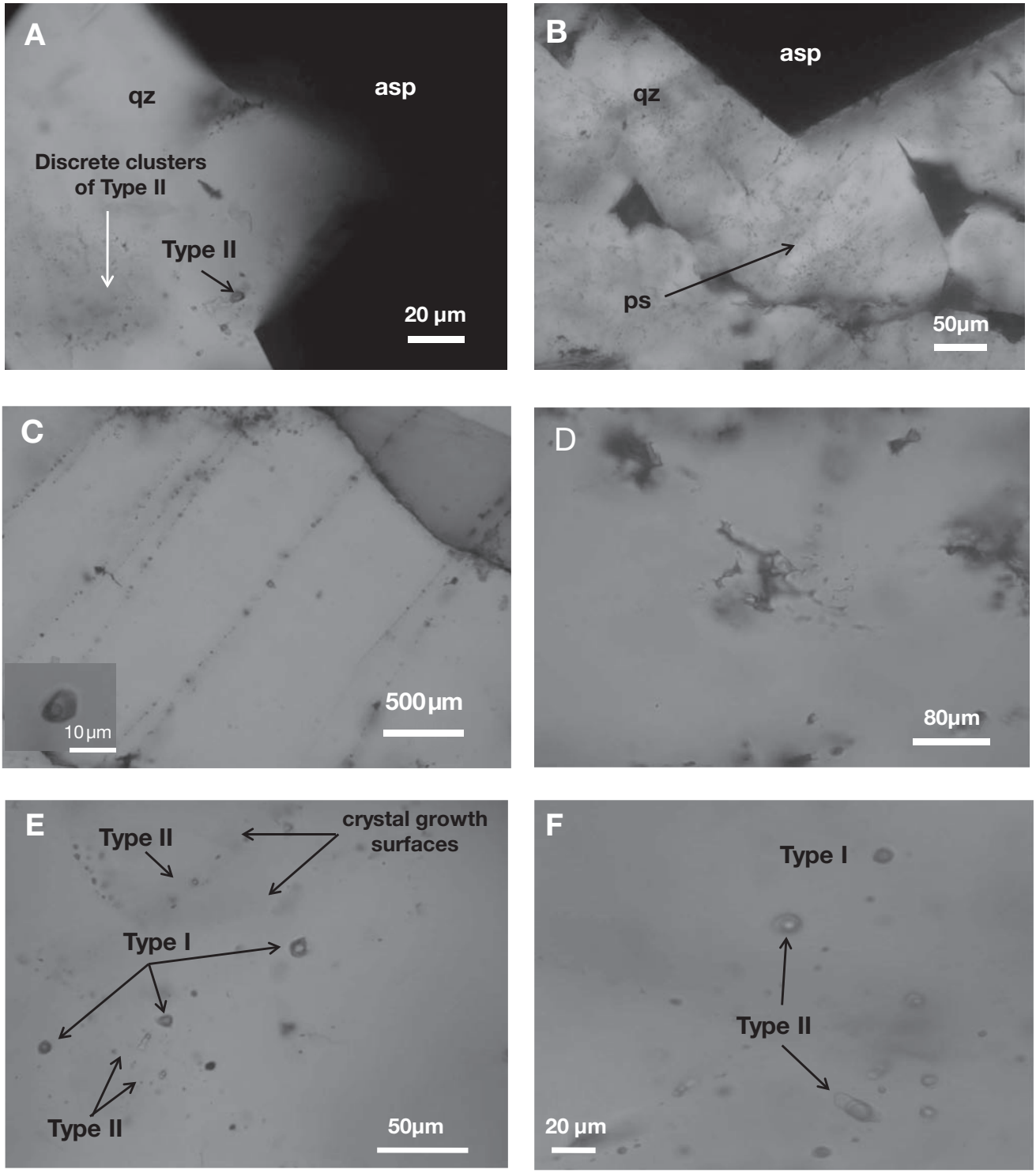


FIG. 12. Photomicrographs in plane polarized light showing selected petrographic relationships and types of fluid inclusions in auriferous samples from Asimotrypes. A. Isolated large primary type II aqueous-carbonic $H_2O$-$CO_2$-NaCl inclusion (black arrow) hosted by jasperoidal quartz-2 (qz) intergrown with gold-bearing arsenopyrite (asp). Discrete clusters (white arrow) of type II inclusions in the centre of quartz crystal defining growth zones indicate primary origin. Note the close relationship between primary type II inclusions and gold-bearing arsenopyrite. B. Primary-pseudosecondary aqueous-carbonic fluid inclusions occurring as discontinuous trails (ps) with variable orientation that mark intragranular healed fractures within individual euhedral quartz-2 crystal intergrown with auriferous arsenopyrite(asp). C. Secondary type IIIb aqueous fluid inclusion trails that transect quartz-2 grain boundaries. Inset shows aqueous two-phase type IIIb inclusion. D. Naturally decrepitated type IV inclusions within quartz-2. E. Type I and II inclusions, within the same field of view that define crystal growth zones of auriferous quartz-2. F. Three-phase primary $H_2O$-$CO_2$-NaCl inclusions (type II) with variable phase ratios (arrows) coexisting with $CO_2$-rich inclusions (type I).

coexist with inclusion types I and II, but mostly they occur as trails along secondary transgranular healed fractures (Fig. 12C).

*Type IV:* These are secondary, naturally decrepitated and/or reequilibrated type I, II, and III inclusions. The term "reequilibration" is used here sensu Vityk and Bodnar (1995) and includes any obvious changes in the inclusion density and/or texture. Type IV includes several subtypes: (1) annular inclusion reequilibration textures of former carbonic and/or aqueous inclusions (Fig. 12D); (2) irregular-shaped decrepitated inclusions which are surrounded by clusters of small, usually regular to rounded satellite inclusions (<3 $\mu$m) (Fig. 12D), indicating postentrapment reequilibration; (3) irregular dendritic and scalloped inclusion textures that point to fluid inclusion decrepitation under isobaric cooling conditions (Fig. 12D).

Combinations of different fluid inclusion types I and II are common within a cluster or intragranular trail, and these constitute distinct fluid inclusion assemblages. Transgranular trails that contain only one fluid inclusion type are observed and exclusively make up type III inclusions.

### *Microthermometry results*

No systematic differences of microthermometric properties were observed between replacement-type (10 samples) and crosscutting vein mineralization (4 samples). Fluid inclusion microthermometric data and calculated fluid properties are summarized in Table 2.

*Type I inclusions:* Final melting temperatures of solid $CO_2$ ($T_{m_{CO_2}}$) in type I inclusions range narrowly from –56.9° to –56.6°C (Fig. 13A), indicating that the carbonic phase in the inclusions is nearly pure $CO_2$. This was also confirmed by bulk volatile analyses (see below). Bubble point homogenization temperatures of the $CO_2$ liquid + vapor phases ($T_{h_{CO_2}}$) range from 26.5° to 29.4°C. No clathrate melting was observed upon heating of frozen type I inclusions. However, these $CO_2$-rich inclusions may contain up to 15 vol percent $H_2O$, even though an $H_2O$ phase is not visible. Bulk densities range from 0.61 to 0.68 g/cm$^3$.

*Type II inclusions:* Final melting temperatures of solid $CO_2$ ($T_{m_{CO_2}}$) in type II inclusions were between –57.1° and –56.6°C (Fig. 13A), indicating almost pure $CO_2$ (confirmed by bulk volatile analyses; see below). Temperatures of $CO_2$ clathrate melting ($T_{m_{clathrate}}$) in the presence of both liquid and vapor $CO_2$ range from 6.1° to 9.7°C (Fig. 13B). The liquid and vapor phases of the carbonic phase exhibited bubble point homogenization $T_{h_{CO_2}}$ between 25.5° and 29.5°C (Fig. 13C), whereas the homogenization temperatures (Th) to both the carbonic and aqueous phases range between 250° and 300°C (Fig. 13E). Homogenization to liquid occurred in the range of 250° to 295°C (median value 280°C) and homogenization to vapor occurred from 275° to 300°C (median value 290°C). Homogenization temperatures in either phase cluster between 250° and 300°C. Some type II inclusions, which have comparatively higher $CO_2$-phase volumes and larger diameters, decrepitated before homogenization at temperatures between 250° and 300°C. Calculated fluid inclusion concentrations of $CO_2$ in the system $H_2O$-$CO_2$-NaCl range from 3 to 54.5 mole percent, with most values concentrating either between 3 and 16.1 or 22.3 and 54.5 mole percent $CO_2$. Bulk salinities range from 0.6 to 7.3 wt percent NaCl equiv, $CO_2$ densities range from 0.65 to 0.70 g/cm$^3$, and bulk densities are from 0.74 to 1.05 gr/cm$^3$.

TABLE 2. Summary of the Microthermometric Data and Calculated Fluid Properties of the Different Fluid Inclusion Types in Auriferous Quartz from Asimotrypes

| Carbonic | Type I | |
|---|---|---|
| System | $CO_2$ (±$H_2O$) | |
| Abundance | Rare | |
| $V_{CO_2}$%[1] | 90–100 | |
| $Tm_{CO_2}$(°C) | –56.6 to –56.9(–56.6) | |
| $Th_{CO_2}$(°C) | +26.5 to + 29.4(+27.9) | |
| Mode[2] | L | |
| $CO_2$ density g/cm$^3$ | 0.61 to 0.68(0.64) | |
| **Aqueous–carbonic** | **Type II** | |
| System | $H_2O$-$CO_2$-NaCl | |
| Abundance | Abundant | |
| $V_{CO_2}$%[1] | 15–85 | |
| $Tm_{CO_2}$(°C) | –56.6 to –57.1(–56.8) | |
| $Tm_{clathrate}$(°C) | + 6.1 to +9.7(+7.9) | |
| Wt % NaCl equiv | 0.6 to 7.3(3.9) | |
| $Th_{CO_2}$(°C) | +25.5 to +29.5(26.5) | |
| $CO_2$ density g/cm$^3$ | 0.65 to 0.70(0.67) | |
| bulk density g/cm$^3$ | 0.74 to 1.05(0.9) | |
| $Th_{total}$ (°C) | 250 to 300(273) | |
| Mode[2] | L,V | |
| **Aqueous** | **Type IIIa** | **Type IIIb** |
| System | $H_2O$-NaCl | $H_2O$-NaCl |
| Abundance | Rare | Abundant |
| $V_g$(%) | 15–25 | 15–25 |
| $T_e$(°C) | –22 to –24 | –22 to –24 |
| $Tm_{ice}$ | –4.8 to –5.9 (–5.35) | –3.5 to –5.9 (4.7) |
| Mass % NaCl equiv | 7.5 to 9(8.25) | 5.6 to 9.1(6.7) |
| Bulk density g/cm$^3$ | 0.95 to 0.98(0.96) | 0.84 to 0.98(0.91) |
| Th (°C) | 248 to 253(250) | 135 to 256(190) |
| Mode[2] | L | L |

Mean values shown in brackets

[1]Degree of filling estimated visually at 30°C from the charts of Shepherd et al. (1985)

[2]Mode of homogenization to the liquid phase (L), or vapor phase (V)

*Type III inclusions:* Temperatures of final ice melting ($T_{m_{ice}}$) range from –5.9° to –3.5°C (median value –4.7°C) (Fig. 13D). Temperatures of homogenization ($T_h$) were between 135° and 256°C and always to the liquid phase (Fig. 13E). Figure 13E shows a bimodal distribution of $T_h$ values which serves as a basis for grouping these inclusions in two subtypes: (1) type IIIa with $T_h$ > 250° (n = 5); and (2) type IIIb with $T_h$ = 130°–250°C (mostly between 150° and 220°C (n = 15). It should be noted that type IIIb inclusions define secondary trails or planes that crosscut grain boundaries. Calculated salinities range from 5.6 to 9.1 wt percent NaCl equiv and bulk densities in the system $H_2O$-NaCl (Bodnar, 1993) from 0.84 to 0.98 g/cm$^3$. A few clathrate melting temperatures were recorded in a small number of type IIIa inclusions between 5° and 9°C suggesting the presence of a possible maximum of 2.2 molal $CO_2$ that would decrease the density by 0.03 to 0.05 g/cm$^3$ (Hedenquist and Henley, 1985).

### *Fluid inclusion gas analyses*

Analytical results for the fluid inclusion volatiles are shown in Table 3. Water is by far the dominant volatile component in the fluid inclusions and typically makes up 85.6 to 98.2

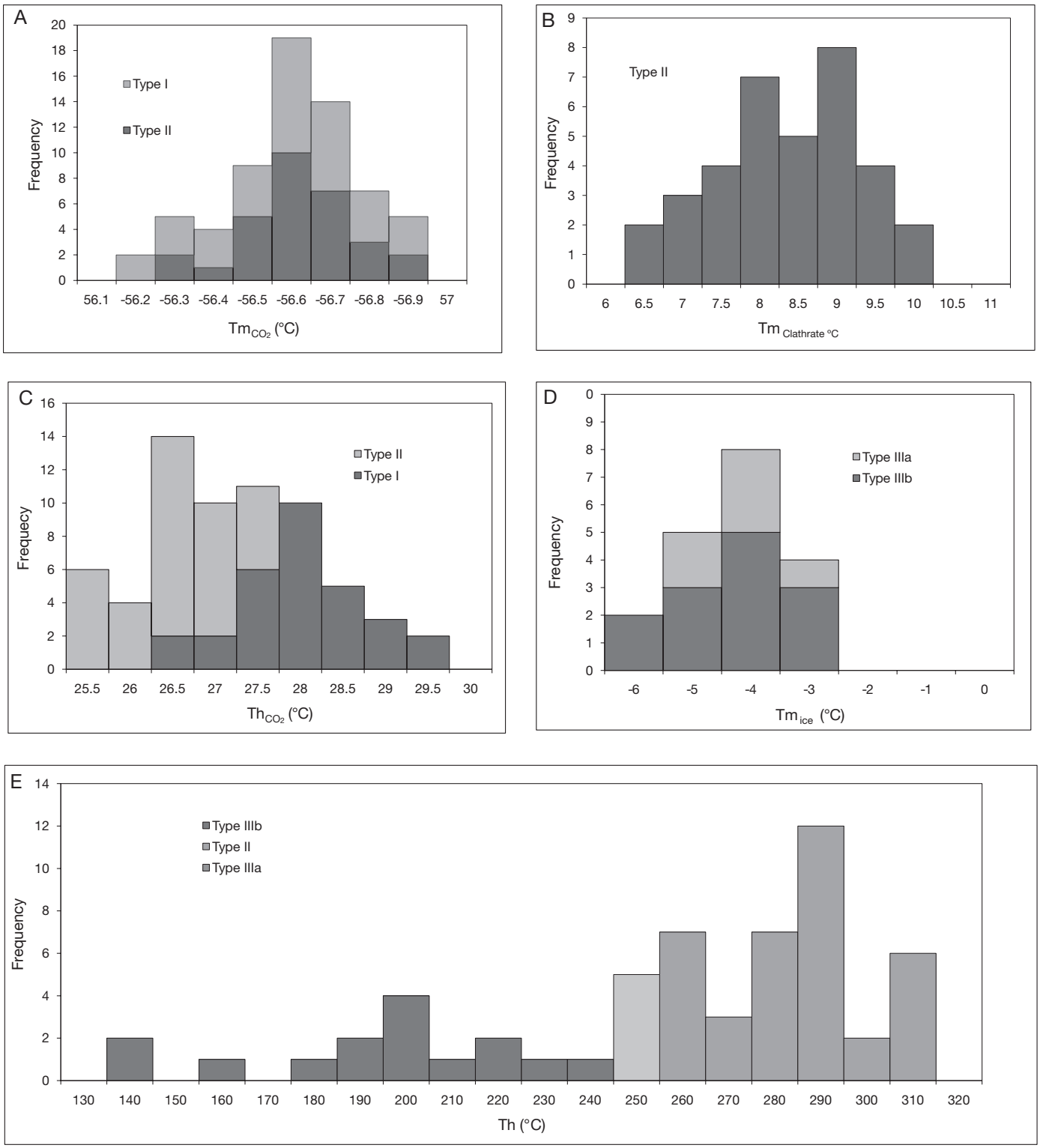


FIG. 13. Frequency histograms of microthermometric data for type I, II, IIIa, and IIIb fluid inclusions. A. $CO_2$ melting ($T_{m_{CO_2}}$). B. Clathrate melting ($T_{m_{clathrate}}$).C. Homogenization of $CO_2$ ($T_{h_{CO_2}}$). D. Final ice melting ($T_{m_{ice}}$). E. Final homogenization ($T_h$).

Table 3. Gas Analyses of Fluid Inclusions Within Gold-Bearing Quartz from Asimotrypes

| | Mole % | | | | | | |
|---|---|---|---|---|---|---|---|
| Sample no. | $N_2$ | $CH_4$ | $CO_2$ | $H_2O$ | Ar | $H_2$ | CO |
| AsO-1 | nd | 0.075 | 2.366 | 96.992 | nd | 0.134 | 0.433 |
| AsO-2 | nd | 0.093 | 1.315 | 98.184 | nd | 0.145 | 0.264 |
| AsO-3 | nd | 0.519 | 1.666 | 96.716 | nd | 0.705 | 0.405 |
| AsO-4 | 0.007 | 0.016 | 4.995 | 94.771 | 0.0027 | 0.320 | 0.289 |
| AsO-6 | 0.057 | 0.008 | 5.161 | 94.245 | nd | 0.325 | 0.205 |
| AsO-7 | nd | 0.202 | 1.621 | 97.845 | nd | 0.050 | 0.283 |
| AsO-8 | 0.182 | 0.014 | 13.739 | 85.592 | 0.0043 | 0.281 | 0.188 |
| AsO-9 | 0.007 | 0.006 | 8.751 | 91.131 | nd | 0.047 | 0.060 |

nd = no data

mole percent of the inclusion fluid; $CO_2$ makes up most of the remaining volatile component, varying between 1.31 to 13.73 mole percent, whereas the other gases—$CH_4$, $N_2$, Ar, $H_2$ and CO—are generally present in amounts smaller than 1 mole percent. This confirms the aqueous nature of mineralizing fluids and provides good agreement with the fluid inclusion microscopic and microthermometric data.

## Stable Isotopes

### *Sulfur isotopes*

No significant variations are observed within the Asimotrypes mineralization; the $\delta^{34}S$ values range narrowly from 2.2 to 3.1 per mil (mean: 2.6 ± 0.3‰ [1$\sigma$; n = 10]) (Table 4).

### *Oxygen, hydrogen, and carbon isotopes*

The $\delta^{18}O$ and $\delta^{13}C$ values of calcite from host marble samples collected along a profile covering a distance from a few centimeters up to 50 m of a mineralized zone explored by the 3K-D adit at Asimotrypes (see Fig. 2), are closely grouped, with a range of 28.1 to 30.9 per mil (median 29.3 ± 0.9‰ [1$\sigma$; n = 15]), and 1.9 and 2.9 per mil (median 2.5 ± 0.3‰), respectively. The oxygen and carbon isotope compositions of the host-rock carbonates are typical of Phanerozoic marine carbonates (–2.0 to +6.0‰; Veizer et al., 1999).

Quartz $\delta^{18}O$ values range from 20.8 to 22.6 per mil, with a mean of 21.9 ± 0.5 per mil (1$\sigma$; n = 10) (Table 4). The quartz-water fractionation of Matsuhisa et al. (1979) was used to derive the oxygen isotope composition of the hydrothermal fluid that equilibrated with quartz at 250° and 300°C, based on fluid inclusion homogenization temperatures. Samples of auriferous quartz were petrographically selected to minimize the percentage of secondary fracture filling type IIIb inclusions. The calculated fluid values range from 11.9 to 13.7 per mil at 250°C and 13.9 to 15.7 per mil at 300°C. The water extracted from fluid inclusions of these quartz samples has $\delta$D values from –105 to –125 per mil, with a mean of –117 ± 7.5 per mil (1$\sigma$; n = 10) (Table 4). These are the first $\delta$D values reported for gold mineralization in the Rhodope Complex. The $\delta^{18}O$ for muscovites range from 12.9 to 14.1 per mil, with a mean value of 13.5 ± 0.5 per mil (1$\sigma$; n = 5) (Table 4). The muscovite-water fractionation equation of Zheng (1993) was utilized to compute the oxygen isotope composition of hydrothermal fluids. The calculated $\delta^{18}O$ values at 300°C range from 10.2 to 11.3 per mil, and 250°C from 11.4 to 12.7 per mil. Quartz-muscovite pairs with textures indicating coprecipitation have $\Delta^{18}O$ values of 6.0 and 6.1 per mil, yielding equilibrium isotopic temperatures of 262° to 268°C, consistent with the average homogenization temperatures of fluid inclusions in auriferous quartz (Fig. 13E).

## Discussion

We believe the geologic, textural, mineralogical, and geochemical features described here support a clearly epigenetic, postmetamorphic, and postmagmatic origin for the Asimotrypes gold mineralization. Our data show that gold mineralization was contemporary with, and genetically related to, Aegean extension and core complex exhumation.

### *Geologic and mineralogical evidence*

The gold mineralization at Asimotrypes is subject to both tectonic as well as lithological control (see Fig. 3). Major ore-controlling factors are the intersection of local zones of porosity and permeability and steep, high-angle faults. Permeable features at Asimotrypes are extensional ductile shear zones (i.e., top-to-the-southwest siliceous mylonites) between rocks of differing lithology (i.e., marbles and mica schists), steep feeder brittle normal faults (i.e., northwest-southeast– to east-west–trending quartz veins), and reactive carbonate rock types (i.e., marbles). Localization of ore may have been enhanced by the less permeable mica schists as aquitards. The mylonite ore-controlling structures are characterized by northeast-southwest–oriented extensional, ductile, flat-lying foliation, with top-to-the-southwest sense of shear, corresponding to the regional northeast-southwest–directed extension that characterizes the whole Southern Rhodope Core Complex. The brittle northwest-oriented feeder structures crosscut the ductile fabrics of the host rocks, and they document a northeast-southwest brittle extension parallel to the regional ductile baric of the host rocks; also, the northeast-southwest brittle extension has controlled the Neogene Strymon basin during the late Miocene and Pliocene, and also strongly imprinted the Messolakia granitoid (15.0 ± 0.3 m.y. cooling age), after the latter was already emplaced and cooled (Tranos et al., 2008; Tranos, 2011). These structural relationships indicate the following: (1) both ductile and brittle structures may be interpreted within a single, continuous extensional and exhumation event, which started with ductile deformation and changed into brittle deformation during exhumation of the core complex (Brun and Sokutis, 2007; Dinter, 1998). Similar

TABLE 4. Stable Isotope Data of Gangue Minerals and Marble Calcite from Asimotrypes

| | | | Silicates | Carbonates | | Fluid inclusions | Sulfides |
|---|---|---|---|---|---|---|---|
| Sample no. | Mineral | Sampling site | $\delta^{18}O$ (‰) | $\delta^{13}C$ (‰) | $\delta^{18}O$ (‰) | $\delta D_{H2O}$ (‰) | $\delta^{34}S$ (‰) |
| AsO-1 | Quartz | Mineralization | +20.8 | | | –125 | |
| AsO-2 | Quartz | Mineralization | +22.1 | | | –105 | |
| AsO-3 | Quartz | Mineralization | +21.4 | | | –110 | |
| AsO-4 | Quartz | Mineralization | +22.6 | | | –120 | |
| AsO-5 | Quartz | Mineralization | +21.9 | | | –115 | |
| AsO-6 | Quartz | Mineralization | +21.6 | | | –122 | |
| AsO-7 | Quartz | Mineralization | +22.2 | | | –125 | |
| AsO-8 | Quartz | Mineralization | +22.5 | | | –111 | |
| AsO-9 | Quartz | Mineralization | +21.7 | | | –123 | |
| AsO-10 | Quartz | Mineralization | +21.8 | | | –125 | |
| AsO-3 | Muscovite | Mineralization | +13.6 | | | | |
| AsO-4 | Muscovite | Mineralization | +12.9 | | | | |
| AsO-5 | Muscovite | Mineralization | +14.1 | | | | |
| AsO-6 | Muscovite | Mineralization | +13.2 | | | | |
| AsO-7 | Muscovite | Mineralization | +13.9 | | | | |
| As-1 | Calcite | Host | | +2.7 | +29.9 | | |
| As-4 | Calcite | Host | | +2.6 | +28.4 | | |
| As-5 | Calcite | Host | | +2.9 | +28.4 | | |
| As-7 | Calcite | Host | | +2.6 | +29.9 | | |
| As-9 | Calcite | Host | | +2.5 | +29.2 | | |
| As-12 | Calcite | Host | | +2.6 | +30.3 | | |
| As-18 | Calcite | Host | | +2.9 | +30.9 | | |
| As-22 | Calcite | Host | | +2.9 | +28.1 | | |
| As-23 | Calcite | Host | | +2.9 | +30.8 | | |
| As-32 | Calcite | Host | | +2.1 | +29.1 | | |
| As-50 | Calcite | Host | | +1.9 | +28.5 | | |
| As-52 | Calcite | Host | | +1.9 | +28.5 | | |
| As-53 | Calcite | Host | | +2.6 | +28.3 | | |
| As-54 | Calcite | Host | | +2.6 | +29.8 | | |
| As-56 | Calcite | Host | | +2.5 | +29.1 | | |
| As-11 | Arsenopyrite/pyrite | Mineralization | | | | | +2.8 |
| As-14 | Pyrite | Mineralization | | | | | +2.7 |
| As-16 | Arsenopyrite/pyrite | Mineralization | | | | | +2.2 |
| As-19 | Arsenopyrite/pyrite | Mineralization | | | | | +2.6 |
| As-21 | Pyrite | Mineralization | | | | | +2.8 |
| As-37 | Arsenopyrite/pyrite | Mineralization | | | | | +3.1 |
| As-44 | Arsenopyrite/pyrite | Mineralization | | | | | +2.4 |
| As-46 | Arsenopyrite/pyrite | Mineralization | | | | | +2.3 |
| As-71 | Pyrite | Mineralization | | | | | +2.9 |
| As-72 | Pyrite | Mineralization | | | | | +2.8 |

ductile-then-brittle evolutions during core complex exhumation have been documented in a number of other extensional tectonic settings (e.g., Lister and Davies, 1989; Moritz et al., 2006), (2) there is a close relationship between gold mineralization and the late extensional brittle structures that have acted as feeder channels to the main mineralized zones and postdated metamorphism, the ductile shear deformation of the host rocks, as well as granitoid intrusion.

Moreover, mineralogical evidence indicates that mineralization is postmetamorphic and synchronous with ductile-then-brittle deformation events: (1) hydrothermal quartz is characterized by brittle as well as ductile microstructures, and gold-bearing arsenopyrite-pyrite by cataclasis and brecciation; brittle failure of mineralized quartz may have generated the abundant healed microfractures occupied by type IIIb aqueous inclusions; (2) hydrothermal silicification, sulfidation, and carbonate dissolution overprint the metamorphic minerals and ductile structures of the core complex host marbles and mica schists; (3) the zonal patterns of gold distribution in arsenopyrite suggest no metamorphic recrystallization of arsenopyrite with concurrent remobilization of gold; any postmineralization remobilization of gold is limited to the oxidation of the sulfide host minerals; and (4) compositional zoning in arsenopyrite may be related to complex unrelated to metamorphism textures like fine banding patterns (compare Fig. 9A, B and Fig. 9C-E). These findings are analogous to those reported by Boiron et al. (1989) and Benzaazoua et al. (2007) in epigenetic gold-bearing arsenopyrites from shallow-emplaced epithermal-like refractory gold ores.

In summary, gold mineralization at Asimotrypes is likely to have been controlled by extensional ductile-then-brittle structures, which are consistent with regional Aegean extension and exhumation of the metamorphic Southern Rhodope Core Complex; consequently, gold mineralization is compatible

with processes associated with middle Eocene to present Aegean extension through the Kerdylion detachment zone. Furthermore, a clearly postmetamorphic and postmagmatic age is indicated for the gold mineralization at Asimotrypes, which is at least younger than the 15.0 ± 0.3 m.y. cooling age of the Messolakia granitoid (Tranos et al., 2008; Tranos, 2011).

*Evidence from fluid inclusions and possible P-T constraints*

The incidence of carbonic, aqueous-carbonic, and aqueous fluid inclusions in the same sample is classically explained by three possible processes (e.g., Zoheir et al., 2008, and references therein): (1) heterogeneous fluid state which may have been derived by fluid unmixing processes of a $H_2O$-$CO_2$-NaCl fluid (Ramboz et al., 1982) followed by heterogeneous entrapment of a $CO_2$-rich phase and a $H_2O$-rich one as carbonic and aqueous-carbonic inclusions, respectively; (2) mixing of fluids from two different sources followed by entrapment of the various mixing combinations as fluid inclusions (e.g., Xavier and Foster, 1999), and/or entrapment of separate and distinct fluids at different times (e.g., Neumayr and Hagemann, 2002); and (3) post-trapping deformation-induced modification influencing fluid inclusions that had formed by entrapment of a homogeneous one-phase fluid at an earlier stage; deformation causes inclusions to leak, decrepitate or reequilibrate, resulting in the preferential loss of $H_2O$ that is entrapped to form the aqueous inclusions, and the synchronous entrapment of $CO_2$-enriched inclusions (Vityk and Bodnar, 1995).

Heterogeneous entrapment after fluid phase unmixing of a primary $H_2O$-$CO_2$-NaCl fluid induced by a drop in P and T in the shear zones, as the mechanism responsible for the formation of inclusion types I, II, and IIIa, is supported by a number of petrographic and microthermometric properties (Ramboz et al., 1982; Roedder, 1984): (1) type I inclusions coexist with type II inclusions and type IIIa inclusions in primary and/or pseudosecondary settings in the same sample, providing evidence that they are related and contemporaneous; (2) aqueous-carbonic type II inclusions are pervasively developed within individual samples and yield highly variable $CO_2$/$H_2O$ phase ratios within individual clusters or internal trails; they homogenized into the $H_2O$ or $CO_2$ phase, or decrepitated, at overlapping temperature ranges between 250° and 300°C (Fig. 13E); (3) temperature of total homogenization $T_h$ vs. salinity plot on Figure 14 shows a "boiling," near-vertical trend of increasing salinity (1–8 wt % NaCl equiv) associated with a gradual decrease in $T_h$ (300°–250°C). The few measured type IIIa fluid inclusions that display $T_h$ values ~250°C, and spatial and textural association with $CO_2$- and $H_2O$-$CO_2$–rich fluid inclusions in gold bearing samples may represent the $H_2O$-rich end member phase resulting from unmixing of the primary $H_2O$-$CO_2$-NaCl fluid (e.g., Boullier et al., 1998). It should be noted that some of the variability of the $CO_2$ content and salinity of type II fluid inclusions at Asimotrypes may be interpreted as a result of carbonate dissolution during marble replacement at the level of gold mineralization, and interaction of low salinity mineralizing fluids with metamorphic silicates (i.e., sericites-illites) in the host impure (cipoline) marble and metasedimentary (detrital) rocks, respectively; the latter can host significant amounts of Cl that can be released during interaction with hydrothermal fluids.

The lack of distinct fluid inclusion populations that have widely variable $T_h$ and equivalent wt percent NaCl values—reflecting variable compositions and temperatures of entrapment (e.g., Xavier and Foster, 1999) and showing a mixing trend—suggests the discharge of the mixing of two separate fluids process as a mechanism for the formation of fluid inclusion types in the studied samples. Equally, deformation-produced post-trapping modification of inclusions originally formed by homogeneous fluid trapping has been dismissed as a mechanism responsible for the formation of all types of fluid inclusions observed, as this would also generate large variations of $CO_2$-phase density in $CO_2$-bearing inclusions, and a wide variability in $T_h$ values. In our samples, primary and pseudosecondary $CO_2$-bearing inclusions exhibit narrow ranges of $CO_2$-phase densities and $T_h$ values (see Table 2). However, $CO_2$-rich type I and, to a lesser extent, $CO_2$-$H_2O$–rich type II inclusions occur in clusters together with type IV naturally decrepitated and/ or apparently empty inclusions. This proximity suggests leakage was responsible for the formation of some of these inclusions from initial $H_2O$-$CO_2$ inclusions due to later crystal deformation. Moreover,

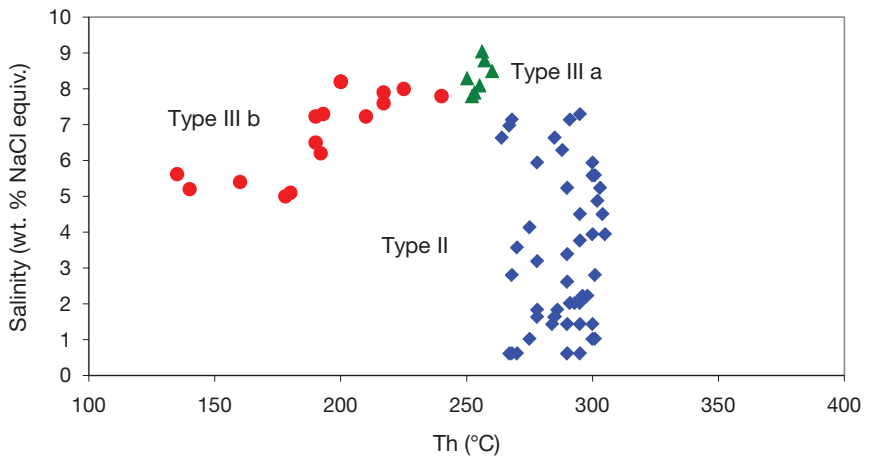


FIG. 14. Binary plot of fluid inclusion homogenization temperature (Th) and calculated salinity for inclusion types II, IIIa, and IIIb. See text for discussion.

type II inclusion isochore distribution may be interpreted as a result of reequilibration under conditions of high internal overpressures (Fig. 15). Isochores scatter from >2 kbars for temperatures of ~270°C, to >4 kbars for temperatures of >300°C. The scatter in inclusion isochores to >2 kbars below the isochore for the densest inclusion indicates a >2 kbars pressure difference between the high-density inclusions and ambient conditions; this may have caused reequilibration of early inclusions, depending on their size (Vityk and Bodnar, 1995). Alternatively, some of the scatter may be a result of fluid unmixing, pressure fluctuations during fluid entrapment, and errors of determining bulk inclusion density from visual estimation from phase proportions (Roedder, 1984; Vityk and Bodnar, 1995).

Fracture-controlled type IIIb fluid inclusions are chemically, physically, and microthermometrically distinct from the $CO_2$-bearing fluid inclusions related to gold-bearing sulfide mineralization and, therefore, those inclusions represent a different hydrothermal fluid event. These fluids are similar to late, low-temperature fracture fillings by distinct low salinity aqueous fluids representing high-level meteoric water introduced during uplift within an extensional core complex (Beaudoin et al., 1992; Marshall et al., 2000; Moritz et al., 2006; Mulch et al., 2007).

Fluid inclusion data demonstrate that chemically similar $H_2O$-$CO_2$-NaCl fluids were responsible for the various stages of silicification, and that heterogeneous phase immiscibility of this fluid was pervasive throughout the Asimotrypes auriferous system. This relationship and the lack of clear textural evidence to point out a large time gap between deposition of the different varieties of quartz indicate that all varieties of quartz in the siliceous auriferous bodies are grossly coeval, and that they form part of the same evolving hydrothermal fluid system that deposited refractory gold and quartz mineralization either as a result of fluid-rock reaction and/or fluid unmixing, or both (e.g., Shelton et al., 2004).

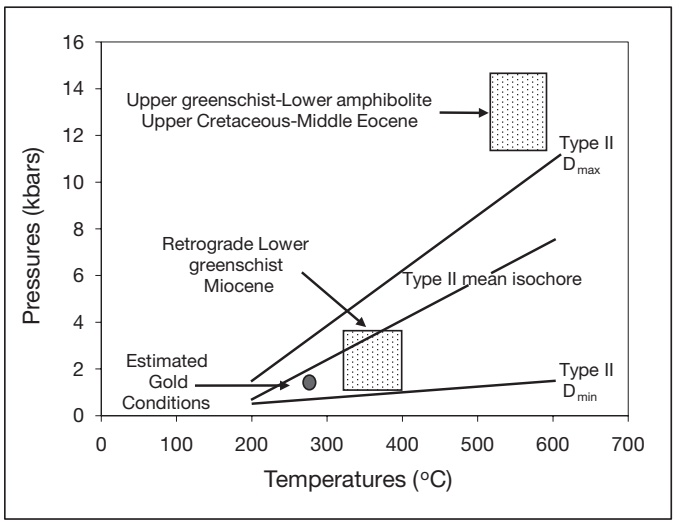


FIG. 15. Pressure-temperature plot showing calculated isochores for type II inclusions, in relation to inferred regional metamorphism in the Southern Rhodope core complex. Oval shows schematically the conditions estimated for phase separation, trapping of type I, II, and IIIa inclusions, and precipitation of auriferous arsenopyrite and pyrite. See text for discussion.

Selecting from fluid unmixing, fluid inclusion reequilibration, and/or fluid/marble interaction as the sole process causing formation of inclusion types I, II, and IIIa is difficult. However, it should be noted that all of these processes may have been operating contemporaneously within one evolving hydrothermal event during a prolonged and progressive extensional deformation episode, and that it was triggered by depressurization due to uplift and extensional core complex exhumation (e.g., Vityk and Bodnar, 1995; Marshall et al., 2000; Kilias, 2001, and references therein). Consequently, the fluid inclusion data, in conjunction with geologic, structural, and quartz textures permit the interpretation that fluid trapping and gold mineralization at Asimotrypes was syndeformational, and took place during depressurization and uplift as a result of exhumation of the Southern Rhodope Core Complex.

If inclusion types I, II, and IIIa are considered to have been trapped during mineralization as immiscible fluids, then measured $T_h$ represents temperatures of immiscibility and maximum trapping temperatures, but only if derived from fluid inclusions that have been carefully selected as having been least influenced by reequilibration and/or leakage (Ramboz et al., 1982; Uemoto et al., 2002; Zoheir et al., 2008). Thus, trapping temperatures are interpreted to be ~270°C, because such $T_h$ has been measured in type II inclusions which show the least amount of scatter, with the same interpretation applicable to $T_{h_{CO_2}}$ values (hence, $CO_2$-phase density) (~27.5°C, Fig. 13C) for the same fluid inclusion assemblage. These latter fluid inclusions are considered to have been the least influenced by deformation (Roedder, 1984; Zoheir et al., 2008). This trapping temperature interpretation is supported by quartz-muscovite pairs, with textures indicating coprecipitation, that have $\Delta^{18}O$ values of 6.0 and 6.1 per mil, yielding equilibrium isotopic temperatures of 262° to 268°C, which are very close to the average homogenization temperatures of fluid inclusions in auriferous quartz ($T_h$ = 270°C, Fig. 13E, Table 2). Moreover, because such type II fluid inclusions are spatially related to gold-bearing sulfide minerals in primary settings at Asimotrypes, their trapping temperatures of ~270°C also represent maximum refractory gold mineralization temperatures. Isochoric calculations for these inclusions show that maximum pressure of trapping and hence minimum pressure of phase separation was ~1.8 to 2 kbars (Fig. 15) consistent with a depth between 6 and 9 km under lithostatic load, or an unlikely >15 km under hydrostatic load.

### *Evidence from stable isotopes and origin of fluids*

Auriferous quartz from Asimotrypes has a narrow range of high $\delta^{18}O$ values (20.8–22.6‰). The calculated $\delta^{18}O_{water}$ values range from 11.9 to 13.7 per mil at 250°C, and 13.9 and 15.7 per mil at 300°C (Matsuhisa et al., 1979). The $\delta D_{water}$ values of fluid inclusion water in auriferous quartz range between –125 and –105 per mil. These values overlap with the $\delta D_{water}$ values of present-day high altitude local meteoric waters ($\delta^{18}O$ = –19.6‰; $\delta D$ = –131.7‰; Dotsika et al., 2010), strongly suggesting that the hydrothermal fluids trapped in the fluid inclusions from auriferous quartz in Asimotrypes were meteoric in origin (e.g., Taylor, 1979). Such very low hydrogen isotope composition of fluid inclusion water ($\delta D_{(fluid\ inclusion\ water)}$ = –135 to –120‰) obtained from Eocene mylonitic quartzite from deep-seated extensional detachment shear

zones of the North American Cordillera, is compatible meteoric waters that infiltrated the ductile segment of the detachment during extensional deformation and exhumation. Moreover, these low meteoric hydrogen isotope values indicate water origin at high elevations (~3,500–4,500 m; Mulch and Chamberlain, 2007, Mulch et al., 2007). In the Greek Rhodope, the occurrence of high paleoelevations at 42 Ma are implied by thermobarometric calculations of amphibolitized eclogites showing P-T conditions of 15 kbars and >800°C, respectively (Baziotis et al., 2008), suggesting considerable thick crust (55–60 km) and hence high altitudes before orogen collapse and core complex formation.

Figure 16 shows measured and calculated fluid compositions from Asimotrypes gold mineralization on a conventional hydrogen versus oxygen isotope diagram. The paired $\delta^{18}O_{water}$ and $\delta D_{water}$ values plot outside both magmatic and metamorphic water boxes, and are indeed consistent with hydrothermal fluids of meteoric water or evolved meteoric water origin that were shifted from the meteoric water line. These isotopic shifts coupled by the narrow range of $\delta^{18}O_{water}$ values (11.9 –15.7‰; 250°–300°C) and the wider range of $\delta D_{water}$ values (–105 to –125‰), are compatible with low volumes of D-depleted hydrothermal fluids of meteoric origin that exchanged with a large reservoir of relatively $^{18}O$-enriched metasedimentary host rocks (Taylor, 1979; Barker et al., 2000; Nutt and Hofstra, 2003). In order to identify whether or not the oxygen and hydrogen water values in our auriferous samples are proof of compositions produced by isotopic exchange of local meteoric water with oxygen and hydrogen in marble country rock, we have modeled the effects of such isotope exchange between meteoric water and Transitional unit marble as a function of water/rock ratio and temperature.

The $\delta^{18}O$ and $\delta^{13}C$ values of calcite from marble country rock not spatially related to mineralization are closely grouped, with a range of 28.1 to 30.9 per mil (median 29.3 ± 0.9‰ [1$\sigma$; n = 10]), and 1.9 and 2.9 per mil (median 2.5 ± 0.3‰), respectively. These values are undepleted in relation to typical marine carbonates (Veizer and Hoefs, 1976; Veizer et al., 1999), and are comparable to the reported values for calcite marbles of other parts of the Southern Rhodope Core Complex (Boulvais et al., 2007). This similarity suggests that the marbles were not significantly changed during metamorphism, but largely retained their original $\delta^{18}O$, $\delta^{13}C$, and highly possibly $\delta D$ isotopic values of the impure limestone protolith. The hydrogen and oxygen isotope composition of water was calculated using the mass balance equations of Field and Fifarek (1985), expressed as follows:

$$\delta D^{f}_{water} = [\delta D^{i}_{rock} - \Delta D_{rock\text{-}water} + \delta D^{i}_{water} \cdot (w/r) \cdot (C H^{i}_{water}/C H^{i}_{rock})] / [1+(w/r) \cdot (C H^{i}_{water}/C H^{i}_{rock})]$$

$$\delta^{18}O^{f}_{water} = [\delta^{18}O^{i}_{rock} - \Delta^{18}O_{rock\text{-}water} + \delta^{18}O^{i}_{water} \cdot (w/r) \cdot (C O^{i}_{water}/C O^{i}_{rock})] / [1+(w/r) \cdot (C O^{i}_{water}/C O^{i}_{rock})]$$

where f = final, i = initial, w/ r = water to rock mass ratio, $CO^{i}_{water}/ CO^{i}_{rock}$ and $CH^{i}_{water}/ CH^{i}_{rock}$ are the ratios of the weight-percent oxygen, and hydrogen, in water to that in rock, before fluid-rock isotope exchange reaction. Using the model constraints, isotopic fractionation factors, equations, and rock compositions set forth below, the final isotopic composition of meteoric water was calculated at water/rock values of 0.01 to 10 and temperatures of 200° and 300°C, in order to

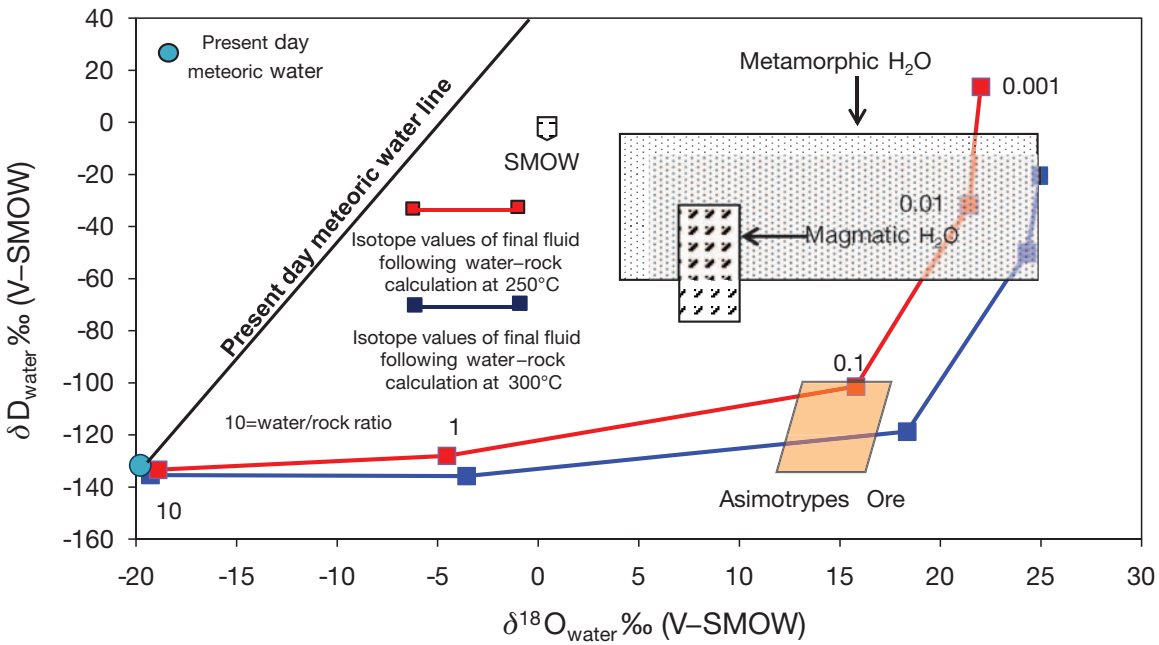


FIG. 16. Plot of Asimotrypes auriferous hydrothermal system in $\delta D_{water}$ vs. $\delta^{18}O_{water}$ space. Calculated water in equilibrium with measured $\delta^{18}O$ for auriferous quartz versus directly measured fluid inclusion $\delta D$ for auriferous quartz compared with VSMOW, magmatic and metamorphic water fields (Sheppard, 1986), and Greek present-day meteoric waters (Dotsika et al., 2010). Water /rock ratio calculations were conducted for final auriferous water isotope compositions using possible marble and starting meteoric water compositions and possible ranges of water/rock ratios, following the method of Field and Fifarek (1985).

reproduce the consequences of water-rock interaction on isotope exchange in the deeper parts of the hydrothermal system (Faure et al., 2002):

- Water contains 88.8 wt percent oxygen (Field and Fifarek, 1985).
- Water contains 11.2 wt percent hydrogen (Field and Fifarek, 1985).
- Marble contains 50 wt percent oxygen, therefore $C\,O^{i}_{water}/C\,O^{i}_{rock} = 88.8/50 = 1.62$.
- Marble contains 0.28 wt percent hydrogen, therefore $C\,H^{i}_{water}/\,C\,H^{i}_{rock} = 11.2/\,0.28 = 40$.
- The measured $\delta^{18}O$ values of the unaltered Transitional unit marbles range between 28.1 and 30.9 per mil (median 29.3 ± 0.9‰; Table 4), $\delta^{18}O_{rock} = 29.3$ per mil.
- A $\delta D_{rock} = -60$‰ value of the unaltered Transitional unit marbles was used, based on the assumption that these rocks had initial hydrogen isotope composition similar to "impure" sedimentary rocks that contain subequal amounts of siliciclastic and carbonate components (Field and Fifarek, 1985).
- The isotopic composition of present-day, high-altitude meteoric water has been used as an approximation of local Tertiary meteoric water, therefore $\delta^{18}O^{i}_{water} = -19.6$‰; $\delta D^{i}_{water} = -131.7$ per mil (Dotsika et al., 2010) $\Delta^{18}O_{rock\text{-}water}$ was assumed to be similar to those of calcite-$H_2O$ (Zheng, 1999; Hu and Clayton, 2003). $\Delta D_{rock\text{-}water}$ was assumed to be similar to those of muscovite-$H_2O$ (Suzuoki and Epstein, 1976), and are calculated as follows for various temperatures: $\Delta^{18}O_{calcite\text{-}water} = 5.79(4.35)$ at 300°C, and 9.77(7.21) at 200°C; $\Delta D_{muscovite\text{-}water} = -48.17$ at 300°C, and –79.61 at 200°C (Zheng, 1999; values in parentheses are from Hu and Clayton, 2003).

The results depicted in Figure 16 indicate that the high fluid $\delta^{18}O$ values (11.9–13.7‰ at 250°C, and 13.9–15.7‰ at 300°C), as calculated from quartz, could have been produced exclusively by water-rock interactions between heated meteoric water and the Transitional unit marbles, at low water/rock ratio. Therefore, the $\delta^{18}O$ and $\delta D$ data from Asimotrypes indicate that the marble interaction is key in shaping the isotope composition of the hydrothermal fluids that were meteoric in origin. A deep meteoric infiltration interpretation of our data is supported by the regional geologic setting of the Asimotrypes gold mineralization that corresponds to a detachment system that controls rock uplift during late-orogenic extension in actively extending regions, which is known to be pathway for meteoric water fluids (e.g., Fricke et al., 1992; Mulch et al., 2004). Deep circulation of meteoric water is also compatible with the widespread precipitation of quartz associated with mineralization at Asimotrypes (Emsbo et al., 2003).

Arsenopyrite and pyrite have overlapping $\delta^{34}S$ values within a narrow range between 2.2 and 3.1 per mil. The $\delta^{34}S$ values calculated for $H_2S$ in equilibrium with pyrite for temperatures of 250° to 300°C are consistent at 1.1 ± 0.3 per mil. This narrow range, the absence of barite, and the Au-As-Ag-Sb geochemical signature indicate that $H_2S$ was the dominant sulfur species in the mineralizing fluid and sulfide complexing of the metals. Sulfur isotope ($\delta^{34}S$) compositions in the –1 to +5 per mil range are typical of a magmatic source, or may reflect sulfur assimilated from country rocks (e.g., Ohmoto and Goldhaber, 1997). The $\delta^{34}S$ values of marble-hosted base metal-sulfide gold deposits associated with detachment faulting and metamorphic core complexes in the Bulgarian Rhodope (i.e., Madan-mean $\delta^{34}S$ value of 4.4‰; Laki-mean $\delta^{34}S$ value of 5.4‰) overlap with those at Asimotrypes (data from Rice et al., 2007). Also, Asimotrypes is hosted by a rock sequence that contains abundant Paleozoic marine metasediments which likely have a considerable range of sulfur isotope composition. On the basis of these data alone, it is not possible to determine if Asimotrypes sulfur is magmatic or incorporated from metasediment host rocks. However, based on the geologic setting and the postmagmatic timing of mineralization, it is suggested that Asimotrypes sulfide mineralization may have integrated sulfur through leaching from metamorphic rocks of the host core complex, and magmatic rocks through fluid/rock interaction. With the available data, it can only be postulated that the source of gold is in the host sequence that consists of abundant Paleozoic marine metasedimentary (marble and mica schist), and interlayered mafic metavolcanic rocks (amphibolite). This is corroborated by homogeneous Pb isotope data of sulfide minerals from marble-hosted base metal-sulfide-gold deposits from the Greek Rhodope which fall within the ratios for the metamorphic core-complex rocks (Vavelidis et al., 1985; Chalkias and Vavelidis, 1988; Kalogeropoulos et al., 1989; Changkakoti et al., 1990; Amov et al., 1991; Frei, 1995; Marchev et al., 2005).

### *Precipitation of gold*

Because primary gold occurs exclusively as submicrocopic gold in arsenopyrite and arsenian pyrite, it may be suggested that one distinct procedure controlled gold precipitation in Asimotrypes (Cline et al., 2005). Based on the geologic, mineralogical, and geochemical data shown here, possible gold-precipitating processes involve cooling, boiling, and fluid-rock reaction, including processes such as carbonate dissolution, silicate alteration, sulfidation (i.e., addition of sulfur) of Fe-bearing rocks and/or arsenopyritization-pyritization of the mineralized rocks (i.e., introduction of Fe, As, and S) (e.g., Hofstra, 1994; Stenger et al., 1998). Because gold occurs in arsenopyrite and arsenian pyrite in replaced wall rocks and open space deposition of these sulfide minerals has not been observed, it is suggested that fluid-rock interaction has been key to gold deposition (Muntean et al., 2011). The presence of $CO_2$ in the mineralizing fluids, in conjunction with evidence for reaction of gold-bearing fluid with marbles that dominate the core complex, may have assisted most favorable hydrothermal transport of gold from source to the site of mineralization (Heinrich, 2005). Carbon dioxide dissolved in the ore fluid may buffer such fluids at near neutral pH conditions where elevated Au concentrations and Au undersaturation could be maintained by complexation with reduced sulfur at any temperature (Heinrich, 2005). Moreover, the key to Au deposition is stabilization of the gold-hosting minerals, compared to a process that favors mineralization of elemental gold or electrum (see also Kesler, 2004). Sulfidation of Fe-bearing marble wall rocks and/or introduction of arsenopyrite/pyrite as important gold-depositing mechanism(s) in Asimotrypes are supported by the positive correlation in gold versus As + S/Fe plots for mineralized samples (Hofstra, 1994) (Fig. 17). Sulfidation of Fe-bearing wall rocks can account for refractory gold mineralization, with Fe concentrations between

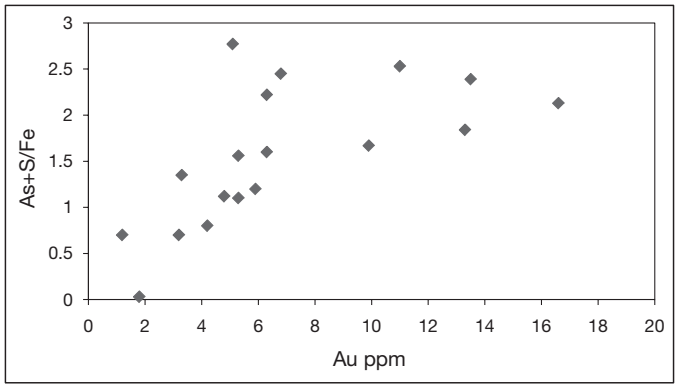


FIG. 17. Relationship between Au grade and As+S/Fe ratio for auriferous samples from Asimotrypes.

0.5 and 2 wt percent (Hofstra, 1994), which are higher compared to the analyzed values in relatively unaltered Transitional unit marble (Fe = 0.03 to 0.77 wt %; App.). Moreover, mineralized samples contain statistically significant higher iron and sulfur compared to country rock outside the mineralized zone, indicating that these increased values are the result of addition of both sulfur and iron to these rocks (App.). Consequently, our preferred interpretation is that gold was precipitated from an $H_2S$-rich ore fluid undersaturated in metallic gold when the host sulfide minerals were stabilized as a result mainly of the addition of pyrite (pyritization), rather than by direct sulfidation of marble wall rock.

*Comparisons with existing gold metallogenic models*

The classification of the Asimotrypes mineralization into existing Au metallogenic models is not clear cut. Many of the Asimotrypes characteristic features contrast with those of carbonate-hosted replacement mineralization—for example, direct connection to igneous activity in a subduction-related continental back-arc environment and high formation temperatures (>300°–680°C; mostly 300°–400°C) (e.g., Gilg, 1996; Megaw, 1998). In addition, despite some geologic and geochemical resemblances, Asimotrypes cannot be classified as an orogenic gold mineralization because the latter takes place within an evolving compressional to transpressional orogen from fluids connected to major mantle-crustal devolatilization, magmatism, and deformation (e.g., Groves et al., 2003; Goldfarb et al., 2005). The Asimotrypes gold mineralization has a tectonic and structural setting in common with mineralization genetically associated with extensional structures and metamorphic core complexes, even though there are important differences in terms of host rocks, alteration mineralogy, and metal inventory (Beaudoin et al., 1991, 1992; Losh et al., 2005; Seidel et al., 2005; Gilg et al., 2006; Moritz et al., 2006). In particular, a comparison of Asimotrypes with the Eocene Muteh Au deposit, Iran, and the Tertiary Eastern Rhodopian sedimentary rock-hosted gold deposits, Bulgaria, discloses a good deal of common characteristics, principally a linkage to late Cenozoic extensional tectonism and core complex exhumation, lithological control by carbonate-rich rocks, structural control by interactive ductile-then-brittle extensional deformation, mineralizing processes dependent on fluid/wall-rock reactions, and the Au-Ag-As (±base metals) geochemical signatures (Marchev et al., 2005; Moritz et al., 2006, Marton et al., 2007, 2010; Noverraz et al., 2007).

## Concluding Remarks: A Potentially New Gold Mineralization Style for the Rhodope Region

The Asimotrypes gold mineralization is hosted by marbles of the Southern Rhodope Core Complex, which is the largest core complex in the Aegean region and probably one of the largest worldwide. Asimotrypes gold mineralization was controlled by interactive deformation, hydrothermal fluid flow, and wall-rock carbonate/ore-fluid reaction processes associated with Eocene northeast-southwest extension of Aegean crust during concurrent decompressive uplift of the Southern Rhodope Core Complex. Hydrothermal fluid pathways and permeability networks were controlled by regional- and local-scale extensional structures; such structures within the metamorphic complex, such as steeply dipping northwest-southeast– to east-west–trending brittle faults, and top-to-the-southwest ductile marble mylonites, have provided highly permeable and porous conduits which concentrated and guided ore-fluid flow from source into the zones of gold mineralization. Gold ore was deposited along these conduits, but chiefly at their intersections, with favorable host stratigraphic horizons such as structural marble-mica schist contacts, and at the expense of marble. Fluid activity may be related to high heat flow sustained by extension and core complex exhumation. Mineralizing fluids were hot (>300°C), $CO_2$-bearing, with sufficient reduced S to transport gold, and variable salinity probably as a result of depressurization-induced unmixing of an initial low- to moderate-salinity fluid, combined with fluid-impure marble reactions. Isotopic studies indicate metamorphic rock equilibrated meteoric mineralizing fluids. Mineralizing fluids silicified, decarbonized, and argillized marble wall rocks, and deposited arsenopyrite and arsenian pyrite containing submicroscopic gold as a result mainly of addition of pyrite (pyritization), than direct sulfidation of marble wall rock. Asimotrypes is marble-hosted extension- and metamorphic core complex exhumation-related submicroscopic gold mineralization, and may represent a potential new gold mineralization style for the Rhodope region. This interpretation of Asimotrypes provides fresh insights on the genesis of the metamorphic core complex-hosted gold mineralizations within the framework of recently developed genetic ideas of hydrothermal gold mineralization, and late orogenic evolution in the Tethyan Eurasian metallogenic belt (Heinrich and Neubauer, 2002; Marchev et al., 2005; Moritz et al., 2006; Marton et al., 2010).

## Acknowledgements

Financial support by the European Union-Brite Euram MA2M-CT90-0015 project is gratefully acknowledged. Thanks are due to T.J. Shepherd, J. Naden, J. Baker, R. Hellingwerf, N. Arvanitidis, J. Chatzipanagis, and M. Varti-Matarangas, who have been involved with this project. Special thanks are due to S. Chryssoulis for the SIMS analyses. The insightful review by J. Naden, is thankfully acknowledged. We are grateful for the detailed corrections, comments, and advice of *Economic Geology* reviewers Stephen Kesler and Adrian Boyce.

## REFERENCES


Amov, B.G., Arvanitides, N.D., and Constantinides, D.C., 1991, Isotopic composition of lead in galenas from some mineralization in Greece and their interpretation: Internal Report, Institute of Geology and Mineral Exploration, Thessaloniki Branch, 10 p.

Baker, J.H., Eliopoulos, D.G., Arvanitides, N.D., and Chatzipanagis, J., 1993, Carbonate-hosted precious and base metal mineralizations in northern Greece: Development of new exploration strategies. Fertile lineaments and regional variations of metallic elements.3.4 The Pangeon-Symvolon regions: Athens, Institute of Geology and Mineral Exploration, Final Report, EEC Project MA2M-CT-90-0015, p. 42–48.

Bakker, R.J., 1999, Adaptation of the Bowers and Helgeson (1983) equation of state to the $H_2O$-$CO_2$-$CH_4$-$N_2$-NaCl system: Chemical Geology, v. 154, p. 225–236.

——2003, Package FLUIDS 1. Computer programs for analysis of fluid inclusion data and for modeling bulk fluid properties: Chemical Geology, v. 194, p. 3–23.

Barker, A.J., Bennet, D.G., Boyce, A.J., and Fallik, A.E., 2000, Retrogression by deep infiltration of meteoric fluids into thrust zones during late-orogenic rapid unroofing: Journal of Metamorphic Geology, v. 18, p. 307–318.

Baziotis, I., Mposkos, E., and Perdikatsis, V., 2008, Geochemistry of amphibolitized eclogites and cross-cutting tonalitic-trondhjemitic dykes in the Metamorphic Kimi Complex in East Rhodope (N.E. Greece): Implications for partial melting at the base of a thickened crust: International Journal of Earth Sciences, v. 97, p. 459–477.

Beaudoin, G., Taylor, B.E., and Sangster, D.F., 1991, Silver-lead-zinc veins, metamorphic core complexes and hydrologic regimes during crustal extension: Geology, v. 19, p. 1217–1220.

——1992, Silver-lead-zinc veins and crustal hydrology during Eocene extension, southeastern British Columbia, Canada: Geochimica and Cosmochimica Acta, v. 56, p. 3513–3529.

Benzaazoua, M., Marion, P., Robaut, F., and Pinto, A., 2007, Gold-bearing arsenopyrite and pyrite in refractory ores: Analytical refinements and new understanding of gold mineralogy: Mineralogical Magazine, v. 71, p. 122–142.

Bestmann, M., Kunze, K., and Matthews, A., 2000, Evolution of a calcite marble shear zone complex on Thassos Island, Greece: Microstructural and textural fabrics and their kinematic significance: Journal of Structural Geology, v. 22, p. 1789–1807.

Bigeleisen, J., Pearlman, M.L., and Prosser, A.C., 1952, Conversion of hydrogenic materials to hydrogen for isotopic analysis: Analytical Chemistry, v. 24, p. 1356–1357.

Bodnar, R.J., 1993, Revised equation and table for determinig the freezing point depression of $H_2O$-NaCl solutions: Geochimica et Cosmochimica Acta, v. 57, p. 683–684.

Boiron, M.C., Cathelineau, M., and Trescases, J.J., 1989, Conditions of gold-bearing arsenopyrite crystallization in the Villeranges basin, Marche-Combrailles shear zone, France: A mineralogical and fluid inclusion study: Economic Geology, v. 84, p. 1340–1362.

Bonev, N., and Beccaletto, L., 2007, From syn- to post-orogenic Tertiary extension in the north Aegean region: constraints on the kinematics in the eastern Rhodope-Thrace, Bulgaria-Greece and the Biga Peninsula, NW Turkey: Geological Society of London, Special Publication, v. 291, p. 113–142.

Bonev, N., Burg, J-P., and Ivanov, Z., 2006, Mesozoic-Tertiary structural evolution of an extensional gneiss dome—the Kesebir-Kardamos dome, eastern Rhodope (Bulgaria-Greece): International Journal of Earth Sciences (Geol Rudschau), v. 95, p. 318–340.

Boni, M., and Large, D., 2003, Nonsulfide zinc mineralization in Europe: An overview. Economic Geology, v. 98, p. 715–729.

Boullier, A.M., Firdaous, K., and Robert, F. 1998, On the significance of aqueous fluid inclusions in gold-bearing quartz vein deposits from the southeastern Abitibi subprovince (Quebec, Canada): Economic Geology, v. 93, p. 216–223.

Boulvais, P., Brun, J-P., and Sokoutis, D., 2007, Fluid circulation related to post-Miocene extension, Thassos Island, North Aegean: Geofluids, v. 7, p. 159–170.

Bowers, T.S., and Helgeson, H.C., 1983, Calculation of the thermodynamic and geochemical consequences of non ideal mixing in the system $H_2O$-$CO_2$-NaCl on phase relations in geologic systems: Equation of state for $H_2O$-$CO_2$-NaCl fluids at high pressures and temperatures: Geochimica et Cosmochimica Acta, v. 47, p. 1247–1275.

Brun, J-P., and Faccenna, C., 2008, Exhumation of high-pressure rocks driven by slab rollback. Earth and Planetary Science Letters, v. 272, p. 1–7.

Brun, J-P., and Sokoutis, D., 2007, Kinematics of the Southern Rhodope Core Complex (North Greece): International Journal of Earth Sciences, v. 96, p. 1079–1099.

Burg, J.P., Ricou, L.E., Ivanov, Z., Codfriaux, I., Dimor, D., and Klain, L., 1996, Syn-metamorphic nappe complex in the Rhodope Massif: Structure and kinematics: Terra Nova, v. 8, p. 6–15.

Chalkias, S., and Vavelidis, M., 1988, Interpretation of lead isotope data from Greek Pb-Zn deposits based on an empirical two-stage model: Bulletin of the Geological Society of Greece, v. 23/2, p. 177–193.

Changkakoti, A., Dimitrakopoulos, R., Gray, J., Krouse, H.R., Krstic, D., Kalogeropoulos, S.I., and Arvanitides, N.D., 1990, Sulphur and lead isotopic composition of sulfide minerals from Thermes and Essimi, Rhodope Massif, Greece: Neues Jahrbuch Mineralogie Abhandlungen, v. 9, p. 413–430.

Chatzipanagis, J., 1991, Geological evolution of the Falakron Mt. area: Unpublished Ph.D. thesis, Greece, Athens Technical University, 179 p.

Chryssoulis, S.L., Cabri, L.J., and Lennard, W., 1989, Calibration of the ion probe for quantitative trace precious metal analyses of ore minerals: Economic Geology, v. 84, p. 1684–1689.

Clayton, R.N., and Mayeda, T.K., 1963, The use of bromine pentafluoride in the extraction of oxygen from oxides and silicates for isotopic analysis: Geochimica et Cosmochimica Acta, v. 27, p. 43–52.

Cline, J.S., 2001, Timing of gold and arsenic sulfide mineral deposition at the Getchell Carlin-type gold deposit, north-central Nevada: Economic Geology, v. 96, p. 75–89.

Cline, J.S., Hofstra, A.H., Muntean, J.L., Tosdal, R.M., and Hickey, K.A., 2005, Carlin-type gold deposits in Nevada: Critical geologic characteristics and viable models: Economic Geology 100th Anniversary Volume, p. 451–485.

Cook, N.J., and Chryssoulis, S.L., 1990, Concentrations of "invisible gold" in the common sulfide minerals: Canadian Mineralogist, v. 28, p. 1–16.

Dinter, D.A., 1998, Late Cenozoic extension of the Alpine collisional orogen, northeastern Greece: Origin of the north Aegean basin: Geological Society of America Bulletin, v. 110, p. 1208–1230.

Dinter, D.A., and Royden, L., 1993, Late Cenozoic extension in northeastern Greece: Strymon Valley detachment system and Rhodope metamorphic core complex: Geology, v. 21, p. 45–48.

Dotsika, E., Poutoukis, D., and Raco, B., 2010, Fluid geochemistry of the Methana peninsula and Loutraki geothermal area, Greece: Journal of Geochemical Exploration, v. 104, p. 97–104.

Duan, Z., Möller, N., and Weare, J.H., 1992, An equation of state for the $CH_4$-$CO_2$-$H_2O$ system: II. Mixtures from 50 to 1000°C and 0 to 1000 bar: Geochimica et Cosmochimica Acta, v. 56, p. 2619–2631.

Duschek, W., Kleinrahm, R., and Wagner, W., 1990, Measurements and correlation of the (pressure, density, temperature) relation of carbon dioxide: II. Saturated-liquid and saturated-vapour densities and the vapor pressure along the entire coexistence curve: Journal of Chemical Thermodynamics, v. 22, p. 841–864.

Eleftheriadis, G., and Koroneos, A., 2003, Geochemistry and petrogenesis of post-collision Pangeon granitoids in central Macedonia, northern Greece: Chemie der Erde, v. 63, p. 364–389.

Eleftheriadis, G., Frank, W., and Petrakakis, K., 1999, $^{40}Ar/^{39}Ar$ geochronology of the Pangeon granitoids, Rhodope unit, northern Greece: European Journal of Mineralogy, v. 11, p. 62–67.

Emsbo, P., Hofstra, A.H., Lauha, E.A., Griffin, G.L., and Hutchinson, R.W., 2003, Origin of high-grade gold ore and source of ore fluid components in the Meikle gold deposit, northern Carlin trend, Nevada: Economic Geology, v. 98, p. 1069–1105.

Faure, K., Matsuhisa, Y., Metsugi, H., Mizota, C., and Hayashi, S., 2002, The Hishikari Au-Ag epithermal deposit, Japan: Oxygen and hydrogen isotope evidence in determining the source of paleohydrothermal fluids: Economic Geology, v. 97, p. 481-498.

Field, C.W., and Fifarek, R.H., 1985, Light stable isotope systematics in the epithermal environment: Reviews in Economic Geology, v. 2, p. 99–128.

Frei, R., 1995, Evolution of mineralizing fluid in the porphyry copper system of the Skouries deposit, northeast Chalkidiki (Greece): Evidence from combined Pb-Sr and stable isotope data: Economic Geology, v. 90, p. 746–762.

Fricke, H.C., Wickham, S.M., and O'Neil, J.R., 1992, Oxygen and hydrogen isotope evidence for meteoric water infiltration during mylonitic deformation and uplift in the Ruby-East Humboldt Range metamorphic core complex, Nevada: Contributions to Mineralogy and Petrology, v. 111, p. 203–221.

Gautier, P., Brun, J.P., Moriceau, R., Sokoutis, D., Martinod, J., and Jolivet, L., 1999, Timing, kinematics and cause of Aegean extension: A scenario based on a comparison with simple analogue experiments: Tectonophysics, v. 315, p. 31–72.

Gilg, H.A., 1996, Fluid inclusion and isotope constraints on the genesis of high-temperature carbonate-hosted Pb-Zn- Ag deposits. Society of Economic Geologists Special Publication 4, p. 501–514.

Gilg, H.A., Boni, M., Balassone, G., Allen, C.R., Banks, D., and Moore, F., 2006 Marble-hosted sulfide ores in the Angouran Zn-(Pb-Ag) deposit, NW Iran: interaction of sedimentary brines with a metamorphic core complex: Mineralium Deposita, v. 41, p. 1–16.

Goldfarb, R.J., Baker, T., Dubé, B., Groves, D.I., Hart, C.J.R., and Gosselin, P., 2005, Distribution, character, and genesis of gold deposits in metamorphic terranes: Economic Geology 100th Anniversary Volume, p. 407–450.

Groves, D.I., Goldfarb, R.J., Robert, F., and Hart, C.J.R., 2003, Gold deposits in metamorphic belts: Overview of current understanding, outstanding problems, future research, and exploration significance: Economic Geology, v. 98, p. 1–29.

Hedenquist, J.W., and Henley, R.W., 1985,The importance of $CO_2$ on freezing point measurement of fluid inclusions: evidence from active systems and implications for epithermal ore deposits: Economic Geology, v. 80, p. 1379–1406.

Heinrich, C.A., 2005, The physical and chemical evolution of the low-salinity magmatic fluids at the porphyry to epithermal transition: A thermodynamic study: Mineralium Deposita, v. 39, p. 864–889.

Heinrich, C.A., and Neubauer, F., 2002, Cu-Au-Pb-Zn-Ag metallogeny of the Alpine-Balkan-Carpathian-Dinaride geodynamic province: Mineralium Deposita, v. 37, p. 533–540.

Higgins, M.D., and Higgins, R., 1996, A geological companion to Greece and the Aegean: New York, Cornell University Press, 256 p.

Hitzman, M.W., 1999, Routine staining of drill core to determine carbonate mineralogy and distinguish carbonate alteration textures: Mineralium Deposita, v. 34, p. 794–798.

Hofstra, A.H., 1994, Geology and genesis of the Carlin-type gold deposits in the Jerritt Canyon district, Nevada: Unpublished Ph.D. dissertation, Boulder, University of Colorado, 719 p.

Hofstra, A.H., and Cline, J.S., 2000, Characteristics and models for Carlin-type gold deposits: Reviews in Economic Geology, v. 13, p.163–220.

Hu, G., and Clayton R. N., 2003, Oxygen isotope salt effects at high pressure and high temperature, and the calibration of oxygen isotope geothermometers: Geochimica et Cosmochimica Acta, v. 67, p. 3227–3246.

Jolivet, L., and Brun J.P., 2008, Cenozoic geodynamic evolution of the Aegean: International Journal of Earth Sciences (Geol Rundsch), 1–30 doi: 10.1007/s00531-008-0366-4.

Kaiser-Rohrmeier, M., Handler, R., von Quadt, A., and Heinrich, C.A., 2004, Hydrothermal Pb-Zn ore formation in the central Rhodopian dome, south Bulgaria: Review and new time constraints from Ar-Ar geochronology: Schweizerische Mineralogische und Petro-graphische Mitteilungen, v. 84, p. 37–58.

Kalogeropoulos, S.I., Kilias, S.P., Bitzios, D.C., Nicolaou, M., and Both, R.A., 1989, Genesis of the Olympias carbonate-hosted Pb-Zn (Au-Ag) sulfide ore deposit, eastern Chalkidiki peninsula, northern Greece: Economic Geology, v. 84, p. 1210–1234.

Kalogeropoulos, S.I., Kilias, S.P., and Arvanitides, N.D., 1996, Physicochemical conditions of deposition and origin of the carbonate-hosted base metal sulfide mineralization, Thermes ore-field, Rhodope Massif, N. Greece: Mineralium Deposita, v. 31, p. 407–418.

Kesler, S.E., 2004, Gold in sulfide minerals and ore deposits: Gangue, v. 83, p. 1–8.

Kilias, S.P., 2001, Genesis of vein quartz deposits in relation to uplift of the Serbo-Macedonian Zone, N. Greece: Evidence from fluid inclusion studies: Chemie der Erde, v. 61, p. 117–139.

Kilias, S.P., Kalogeropoulos, S.I., Konnerup-Madsen, J., 1996, Fluid inclusion evidence for the physicichemical conditions of sulphide deposition in the Olympias carbonate-hosted Pb-Zn (Au, Ag) sulphide ore deposit, E. Chalkidiki peninsula, N. Greece: Mineralium Deposita, v. 31, p. 394–406.

Kretchmar, U., and Scott, S.D., 1976, Phase relations involving arsenopyrite in the system Fe-arsenian-S and their application: Canadian Mineralogist, v. 14, p. 364–386.

Kyriakopoulos, K., Pezzino, A., and Moro, A.D., 1989, Rb-Sr geochronological, petrological and structural study of the Kavala plutonic complex (N. Greece): Bulletin of the Geological Society of Greece, v. 23, p. 545–560.

Lescuyer, J.L., Bailly, L., Cassard, D., Lips, A.L.W., Piantone, P., and McAlister, M., 2003, Sediment-hosted gold in south-eastern Europe: The epithermal deposit of Perama, Thrace, Greece: *in* Eliopoulos, D.G., et al., eds., 7th Biennial SGA Meeting, Mineral Exploration and Sustainable Development, Athens, Greece, Rotterdam, Millpress, Proceedings, v. 1, p. 499–502.

Liati, A., 2005, Identification of repeated Alpine (ultra) high-pressure metamorphic events by U-Pb SHRIMP geochronology and REE geochemistry of zircon: the Rhodope zone of Northern Greece: Contributions to Mineralogy and Petrology, v. 150, p. 608–630.

Lips, A.L.W., 2002, Correlating magmatic-hydrothermal ore deposit formation with geodynamic processes in SE Europe: Geological Society of London, Special Publications, v. 204, p. 69–79.

Lister, G., and Davies, G., 1989, The origin of metamorphic core complexes and detachment faults formed during Tertiary continental extension in the northern Colorado River region, USA: Journal of Structural Geology, v. 11, p. 65–94.

Losh, S., Purvance, D., Sherlock, R., and Jowett, E.C., 2005, Geologic and geochemical study of the Picacho gold mine, California: Gold in a low-angle normal fault environment: Mineralium Deposita, v. 40, p. 137–155.

Marchev, R., Kaiser-Rohrmeier, M., Heinrich, C.A., Ovtcharova, M., von Quadt, A., and Raicheva, R., 2005, Hydrothermal ore deposits related to post-orogenic extensional magmatism and core complex formation: The Rhodope Massif of Bulgaria and Greece: Ore Geology Reviews, v. 27, p. 53–89.

Marshall, J., Fisher, D., and Gardner, T., 2000, Central Costa Rica deformed belt: Kinematics of diffusen faulting across the western Panama block: Tectonics, v. 19, p. 468–492.

Marton, I., Moritz, R., Bonev, N., and Marchev, P., 2007, Regional to local ore controls on the formation of sedimentary rock-hosted gold deposits from the eastern Rhodopes, Bulgaria, *in* Andrew, C.J., et al., eds., Digging Deeper: 9th Biennial SGA Meeting, Dublin, Ireland, Proceedings, v. 1, p. 137–140.

Marton, I., Moritz, R., and Spikings, R., 2010, Application of low-temperature thermochronology to hydrothermal ore deposits: formation, preservation and exhumation of epithermal gold systems from the eastern Rhodopes, Bulgaria: Tectonophysics, v. 483, p. 240–254.

Matsuhisa, Y., Goldsmith, J.R., and Clayton, R.N., 1979, Oxygen isotopic fractionation in the system quartz-albite-anorthite-water: Geochimica et Cosmochimica Acta, v. 43, p. 1131–1140.

McCrea, J.M., 1950, On the isotope chemistry of carbonates and a paleotemperature scale: Journal of Chemistry and Physics, v. 18, p. 849–857.

Megaw, P.K.M., 1998, Carbonate-hosted Pb-Zn-Ag-Cu-Au replacement deposits: An exploration perspective, *in* Lentz, D.R., ed., Mineralized intrusion-related skarn systems: Mineralogical Association of Canada Short Course Series, v. 26, p. 337–358.

Melfos, V., Vavelidis, M., Christofides, G., and Seidel, E., 2002, Origin and evolution of the Tertiary Maronia porphyry copper-molybdenum deposit, Thrace, Greece: Mineralium Deposita, v. 37, p.648–668.

Monster, J., and Rees, C.E., 1975, Sulfur isotope secondary standards: Interlaboratory comparisons and discussion. Internal Report, Hamilton, Ontario, Canada, McMaster University.

Moritz, R., Ghazban, F., and Singer, B.S., 2006, Eocene gold ore formation at Muteh, Sanan-daj-Sirjan Tectonic Zone, western Iran: A result of late-stage extension and exhumation of metamorphic basement rocks within the Zagros orogen: Economic Geology, v. 101, p. 1497–1524.

Mposkos, E.D., and Kostopoulos, D., 2001, Diamond, former coesite and supersilicic garnet in metasedimentary rocks from the Greek Rhodope: A new ultrahigh-pressure metamorphic province established: Earth and Planetary Science Letters, v. 192, p. 497–506.

Mulch, A. and Chamberlain, C.P., 2007, Stable isotope paleoaltimetry in orogenic belts—the silicate record in surface and crustal geological archives: Reviews in Mineralogy and Geochemistry, v. 66, p. 89–118.

Mulch, A., Teyssier, C., Cosca, M.A., Vanderhaeghe, O., and Vennemann, T., 2004, Reconstructing paleoelevation in eroded orogens: Geology, v. 32, p. 525–528.

Mulch, A., Teyssier, C., Cosca. M.A., and Chamberlain, C.P., 2007, Stable isotope paleoal-timetry of Eocene core complexes in the North American Cordillera: Tectonophysics, v. 26, TC4001, doi: 10.1029/2006TC001995, 2007.

Muntean, J.L., Cline, J.S., Simon, A.C., and Longo, A.A., 2011, Magmatic-hydrothermal origin of Nevada's Carlin-type gold deposits: Nature Geoscience, doi:10.1038/ngeo1064.

Nader, F.H., Swennen, R., and Keppens, E., 2008, Calcitization/dedolomitization of Jurassic dolostones (Lebanon): Results from petrographic and sequential geochemical analyses: Sedimentology, v. 55, p. 1467–1485.

Nebel, M.L., Hutchinson, R.W., and Zartman, R.E., 1991, Metamorphism and polygenesis of the Madem Lakkos polymetallic sulfide deposit, Chalkidiki, Greece: Economic Geology, v. 86, p. 81–105.

Neumayr, P., and Hagemann, S.G., 2002, 'Hydrothermal Fluid Evolution within the Cadillac tectonic zone, Abitibi greenstone belt, Canada: Relationship to auriferous fluids in adjacent second- and third-order shear zones: Economic Geology, v. 97, p. 1203–1225.

Nitsopoulos, G., 1980, Report on the exploration works carried out at Asimotrypes in 1980: Internal Report, Bauxite Parnassus Mining Co. S.A., 10 p.

Noverraz, C., Moritz, R., Fontignie, D., Kolev, K.,Marchev, P., Vennemann, T., Spangenberg, J.,2007, The Stremtsi gold prospect: A sedimentary rock-hosted, low sulfidation epithermal system in the Tertiary eastern Rhodopes, Bulgaria, *in* Andrew et al., eds., Digging Deeper: 9th Biennal SGA Meeting, Dublin, Ireland, Proceedings, p. 141–145.

Nutt, C.J., and Hofstra, A.H., 2003, Alligator Ridge district, east-central Nevada: Carlin-type gold mineralization at shallow depths: Economic Geology, v. 98, p. 1225–1241.

Ohmoto, H., and Goldhaber, M.B., 1997, Sulphur and carbon isotopes, 3rd ed., *in* Barnes, H.L., ed., Geochemistry of hydrothermal deposits: New York, John Wiley and Sons, p. 517–612.

Perraki, M., Proyer, A., Mposkos, E., Kindly, R., and Hoinkes, G., 2006, Raman micro-spectroscopy on diamond, graphite and other carbon polymorphs from the ultrahigh-pressure metamorphic Kimi complex of the Rhodope metamorphic province, NE Greece: Earth and Planetary Science Letters, v. 241, p. 672–685.

Pracejus, B., 2008, The ore minerals under the microscope, *in* Pracejus, B., ed., Atlases in geosciences: Berlin, Elsevier, 875 p.

Putnis, A. , 2009, Mineral replacement reactions: Reviews in Mineralogy and Geochemistry, v. 70, p. 87–124.

Ramboz, C., Pichavant, M., and Weisbrod, A., 1982, Fluid immiscibility in natural processes: use and misuse of fluid inclusion data in terms of immiscibility: Chemical Geology, v. 37, p. 29–48.

Rice, C., McCoyd, R.J., Boyce, A., and Marchev, P., 2007, Stable isotope study of the mineralization and alteration in the Madjarovo Pb-Zn district, Bulgaria: Mineralium Deposita, v. 42, p. 691–713.

Ricou, L.E., Burg, J.P., Godfriaux, I., and Ivanov, Z., 1998, Rhodope and Vardar: The metamorphic and the olistostromic paired belts related to the Cretaceous subduction under Europe: Geodinamica Acta, v. 11, p. 285–309.

Roedder, E., 1984, Fluid inclusion evidence bearing on the environments of gold deposition, *in* Foster, R.P., ed., Gold '82—the geology, geochemistry and genesis of gold deposits: Rotterdam, Balkema, p. 129–164.

Sagui, C.L., 1930, Economic geology and allied sciences in ancient times: Economic Geology, v. 25, p. 65–86.

Seidel, M., Pack, A., Sharp, Z.D., and Seidel, E., 2005, The Kakopetros and Ravdoucha iron-oxide deposits, western Crete, Greece: Fluid transport and mineralization within a detachment zone: Economic Geology, v. 100, p. 165–174.

Shaw, A.J., and Constantinides, D.C., 2001, The Sappes gold project: Bulletin of the Geological Society of Greece, v. 24 (3), p. 1073–1080.

Shelton, K.L., McMenamy, T.A., van Hees, E.H.P., and Falck, 2004, Deciphering the complex fluid history of a greenstone-hosted gold deposit: Fluid inclusion and stable isotope studies of the Giant mine, Yellowknife, Northwest Territories, Canada: Economic Geology, v. 99, p. 1643–1663.

Shepherd, T.J., Rankin, A.H., and Alderton, D.H.M., 1985, A practical guide to fluid inclusion studies: Glasgow, Blackie and Son, 239 p.

Sheppard, S.M.F., 1986, Characterization and isotopic variations in natural waters: Reviews in Mineralogy, v. 16, p. 165–183.

Sokoutis, D., Brun, J., Van Den Driessche, Pavlidis, S., 1993, A major Oligocene-Miocene detachment in southern Rhodope controlling north Aegean extension: Journal of the Geological Society of London, v. 150, p. 243–246.

Span, R., and Wagner, W., 1996, A new equation of state for carbon dioxide covering the fluid region from the triple-point temperature to 1100 K at pressures up to 800 MPa: Journal of Physics and Chemical Reference Data, v. 25, p. 1509–1596.

Stenger, D. P., Kesler S.E., Peltonen , D.R., and Tapper, C .J., 1998, Deposition of gold in Carlin-type gold deposit: The role of sulfidation and decarbonatization at Twin Creeks, Nevada: Economic Geology, v. 93, p.201–216.

Taylor, H.P., Jr., 1979, Oxygen and hydrogen isotope relationships in hydrothermal mineral de-posits, *in* Barnes, H.L., ed., Geochemistry of ore deposits: New York, Wiley, p. 236–277.

Taymaz, T., Yilmaz, Y., and Dilek, Y., 2007, The geodynamics of the Aegean and Anatolia: introduction: Geological Society of London, Special Publications, v. 291, p. 1–16.

Tranos, M.D., 2010, Strymon and Strymonikos Gulf basins (northern Greece): Implications on their formation and evolution from faulting: Journal of Geodynamics, v. 51, p. 285–305. doi:10.1016/j.jog.2010.10.002.

Tranos, M.D., Kachev, V.N., and Mountrakis, D.M., 2008, Transtensional origin of the NE-SW Simitli basin along the Strouma (Strymon) lineament, SW Bulgaria: Journal of Geological Society London, v. 165, p. 499–510.

Turpaud, P., and Reischmann, T., 2009, Characterization of igneous terranes by zircon dating: implications for UHP occurrences and suture identification in the Central Rhodope, northern Greece: International Journal of Earth Sciences, doi: 10.1007/s00531–008–0409–x.

Uemoto, T., Ridley, J., Mikucki, E., Groves, D.I., and Kusakabe, M., 2002, Fluid chemical evolution as a factor in controlling the distribution of gold at the Archean Golden Crown lode gold deposit, Murchison province, Western Australia: Economic Geology, v. 97, p. 1227–1248.

Varti-Matarangas, M.,and Eliopoulos, D., 2005, Petrographical and stable isotope (C, O) studies of the Pangeon Mountain marbles, northern Greece: Association to host mineralization, *in* Mao, J., and Frank P. Bierlein, F.P., eds., 8th SGA Biennial Meeting, Mineral Deposit Research: Meeting the Global Challenge, Beijing, China, Berlin Freiberg, Springer-Verlag, v. 2, p. 931–934.

Vavelidis, M., Basiakos, I., Begeman, F., Patriarcheas, K., Pernicka, E., Schmitt-Strecker, S., and Wagner, G. A., 1985, Geologie und Erzvorkommen del insel Sifnos, *in* Wagner, G.A., and Weisgerber, G., eds., Silber, Blei, und Gold auf Sifnos; Praehistorische und antike Metallproduktion: Bochum, Der Anschnitt, Beiheft 3, p. 59–80.

Veizer, J., and Hoefs, J., 1976, The nature of $^{18}O/^{16}O$ and $^{13}C/^{12}C$ secular trends in sedimentary carbonate rocks: Geochimica et Cosmochimica Acta, v. 40, p. 1387–1395.

Veizer, J., Ala, D., Azmy, K., Bruckschen ,P., Buhl, D., Bruhn, F., Carden, G.A.F., Diener, A., Ebneth, S., Godderis, Y., Jasper, T., Korte ,G., Pawellek, F., Podlaha, O.G., and Strauss, H., 1999, $^{87}Sr/^{86}Sr$, $\delta^{13}C$ and $\delta^{18}O$ evolution of Phanerozoic seawater: Chemical Geology, v. 161, p. 59–88.

Vityk, M.O., and Bodnar,. R.J., 1995, Do fluid inclusions in high-grade metamorphic terranes preserve peak equilibration density during retrograde decompression?: American Mineralogist, v. 80, p. 641–644.

Voudouris, P., Tarkian, M., and Arikas, K., 2006, Mineralogy of Te-bearing epithermal ores in the Kassiteres-Sappes area, western Thrace, Greece: Mineralogy and Petrology, v. 87, p. 31–52.

Xavier, R.P., and Foster, R.P., 1999, Fluid evolution and chemical controls in the gold deposit of Fazenda Maria Preta, Rio Itapicuru greenstone belt, Bahia, Brazil: Chemical Geology, v. 154, p. 133–154.

Xidas, S., 1984, Geological map of Greece; Nikisiani sheet, scale 1:50,000: Athens, Greece: IGME.

Zhang, Y.G., and Frantz, J.D., 1987, Determination of the homogenization temperatures and densities of supercritical fluids in the system NaCl-KCl-$CaCl_2$-$H_2O$ using synthetic fluid inclusions: Chemical Geology, v. 64, p. 335–350.

Zheng, Y-F., 1993, Calculation of oxygen isotope fractionation in hydroxyl-bearing silicates: Earth and Planetary Science Letters, v. 120, p. 247–263.

——1999, Oxygen isotope fractionation in carbonate and sulphate minerals: Geochemical Journal, v. 33, p. 109–126.

Zoheir, B.A., El-Shazly, A.K., Helba, H., Khalil, K.I., and Bodnar, R.J., 2008, Origin and evolution of the Um Egat and Dungash orogenic gold deposits, Egyptian Eastern Desert: Evidence from fluid inclusions in quartz: Economic Geology, v. 103, p. 405–424.

## APPENDIX

Geochemical Data of Representative and Variably Mineralized Rocks from Asimotrypes

| Sample no. | As-18 | As-22 | As-23 | As-24 | As-26 | As-27 | As-30 | As-50 | As-51 | As-52 | As-54 | As-01 | As-04 | As-05 | As-07 | As-09 | As-12 | As-32 | As-53 |
|---|---|---|---|---|---|---|---|---|---|---|---|---|---|---|---|---|---|---|---|
| Rock | MWR | MWR | MWR | MWR | MWR | MWR | MWR | MWR | MWR | MWR | MWR | MWR | MWR | MWR | MWR | MWR | MWR | MWR | MWR |
| Major elements (wt %) | | | | | | | | | | | | | | | | | | | |
| $SiO_2$ | 0.70 | 1.81 | 6.00 | 3.50 | 3.68 | 2.00 | 1.20 | 1.20 | 0.70 | 0.30 | 0.50 | 22.59 | 15.53 | 15.19 | 18.20 | 20.71 | 29.00 | 28.50 | 21.50 |
| $TiO_2$ | n.d | n.d | 0.03 | n.d | n.d | n.d | n.d | n.d | n.d | n.d | n.d | n.d | n.d | n.d | n.d | n.d | 0.01 | 0.11 | n.d |
| $Al_2O_3$ | 0.08 | 0.46 | 1.05 | 1.00 | 0.75 | 0.55 | 0.26 | 0.25 | 0.22 | 0.05 | 0.12 | 0.66 | 0.54 | 1.38 | 0.47 | 0.40 | 1.31 | 2.95 | 0.50 |
| $Fe_2O_3$ | 0.04 | 0.67 | 1.46 | 0.93 | 0.93 | 0.47 | 0.19 | 0.13 | 0.25 | 0.00 | 1.11 | 1.99 | 0.45 | 1.55 | 0.32 | 0.22 | 1.01 | 1.83 | 0.41 |
| MgO | 0.57 | 1.31 | 3.61 | 5.50 | 1.47 | 4.20 | 15.50 | 0.64 | 20.50 | 1.20 | 20.20 | 1.17 | 1.02 | 1.23 | 1.40 | 0.88 | 1.28 | 1.32 | 0.78 |
| MnO | 0.02 | 0.05 | 0.03 | 0.07 | 0.10 | 0.03 | 0.04 | 0.02 | 0.05 | 0.01 | 0.32 | 1.04 | 0.08 | 0.05 | 0.02 | 0.03 | 0.04 | 0.05 | 0.06 |
| CaO | 54.00 | 51.80 | 46.50 | 45.10 | 49.60 | 48.50 | 36.30 | 53.00 | 31.20 | 54.70 | 31.50 | 39.08 | 45.30 | 44.40 | 43.50 | 42.00 | 37.20 | 34.95 | 42.00 |
| $K_2O$ | 0.04 | 0.09 | 0.15 | 0.22 | 0.13 | 0.10 | 0.07 | 0.05 | 0.06 | 0.01 | 0.01 | 0.19 | 0.11 | 0.51 | 0.18 | 0.17 | 0.55 | 1.06 | 0.19 |
| $Na_2O$ | 0.11 | 0.07 | 0.24 | 0.09 | 0.04 | 0.05 | 0.05 | 0.08 | 0.06 | 0.09 | 0.06 | 0.07 | 0.06 | 0.10 | 0.10 | 0.11 | 0.13 | 0.31 | 0.06 |
| $P_2O_5$ | 0.18 | 0.15 | 0.47 | 0.48 | 0.03 | 0.09 | 0.02 | 0.01 | 0.02 | 0.02 | 0.01 | 0.04 | 0.03 | 0.02 | 0.03 | 0.03 | 0.04 | 0.05 | 0.02 |
| LOI | 43.00 | 42.70 | 39.30 | 42.30 | 42.00 | 42.80 | 45.20 | 43.00 | 46.50 | 43.20 | 46.50 | 31.90 | 37.00 | 36.10 | 35.50 | 35.10 | 27.80 | 25.50 | 33.80 |
| Total | 98.74 | 99.11 | 98.84 | 99.19 | 98.73 | 98.79 | 98.83 | 98.38 | 99.56 | 99.58 | 100.33 | 98.73 | 100.12 | 100.53 | 99.72 | 99.65 | 98.37 | 96.63 | 99.32 |
| Trace elements (ppm) except Au (ppb) | | | | | | | | | | | | | | | | | | | |
| Au | 20 | 30 | 80 | 10 | 40 | n.d | 150 | 80 | 20 | 10 | 60 | 170 | 70 | 90 | 60 | 160 | 670 | 40 | 110 |
| Ag | 11.70 | 11.00 | 8.50 | 9.30 | 9.80 | 9.50 | 7.00 | 9.70 | 6.00 | 9.00 | 5.80 | 17.00 | 26.00 | 12.50 | 8.60 | 9.00 | 8.30 | 6.20 | 7.60 |
| Pb | 6 | 12 | 7 | 10 | 15 | 7 | 8 | 6 | 10 | 5 | 24 | 3205 | 210 | 36 | 10 | 5 | 8 | 12 | 5 |
| Zn | 12 | 26 | 19 | 35 | 19 | 28 | 34 | 9 | 30 | 11 | 24 | 2465 | 85 | 72 | 11 | 5 | 20 | 27 | 7 |
| Cu | n.d | n.d | n.d | n.d | n.d | 5 | n.d | n.d | n.d | n.d | n.d | n.d | n.d | n.d | n.d | n.d | n.d | n.d | n.d |
| As | 163 | 508 | 1364 | 203 | 331 | 72 | 28 | 46 | 22 | 7 | 25 | 1465 | 118 | 94 | 18 | 5 | 998 | 28 | 7 |
| Sb | n.d | n.d | n.d | n.d | n.d | n.d | n.d | n.d | n.d | n.d | n.d | n.d | n.d | n.d | n.d | n.d | n.d | n.d | n.d |
| Bi | n.d | 1 | 1 | 1 | n.d | n.d | 1 | 1 | n.d | 1 | 1 | 1 | 1 | 1 | 1 | 1 | n.d | 1 | 1 |
| Se | n.d | 1 | 1 | 1 | n.d | n.d | 1 | 1 | n.d | 1 | 1 | 1 | 1 | 1 | 1 | 1 | n.d | 1 | 1 |
| Te | n.d | 3 | 3 | 3 | n.d | n.d | 3 | 3 | n.d | 3 | 3 | 3 | 3 | 3 | 3 | 3 | n.d | 3 | 3 |
| Cr | 1 | 7 | 50 | 11 | 29 | 8 | 2 | 1 | n.d | n.d | 3 | 30 | 24 | 9 | 14 | 8 | 18 | 69 | 10 |
| Ni | 1 | 10 | 27 | 21 | 20 | 13 | 5 | 5 | 4 | 4 | 2 | 8 | 5 | 9 | 7 | 4 | 2 | 55 | 6 |
| Co | 39 | 34 | 37 | 37 | 29 | 34 | 33 | 32 | 32 | 29 | 38 | 62 | 56 | 50 | 50 | 59 | 67 | 48 | 44 |
| V | n.d | 5 | 9 | 10 | 3 | 4 | 2 | n.d | n.d | n.d | n.d | 6 | 1 | 6 | n.d | 1 | 7 | 15 | 1 |
| Rb | n.d | 10 | 7 | 6 | 2 | 3 | 1 | n.d | n.d | n.d | n.d | n.d | 2 | 11 | 1 | n.d | 10 | 40 | 1 |
| Sr | 160 | 175 | 226 | 252 | 210 | 226 | 172 | 135 | 30 | 145 | 35 | 247 | 244 | 188 | 280 | 212 | 171 | 248 | 175 |
| Zr | 12 | 11 | 19 | 14 | 18 | 12 | 11 | 12 | 9 | 10 | 7 | 13 | 13 | 24 | 11 | 13 | 20 | 43 | 11 |
| Y | 11 | 11 | 7 | 10 | 4 | 6 | 5 | 6 | 5 | 6 | 3 | 5 | 18 | 13 | 18 | 15 | 19 | 17 | 11 |
| Nb | 1 | 1 | 2 | 2 | 1 | 1 | 1 | 1 | 1 | 2 | 1 | 2 | 2 | 3 | 2 | 2 | 2 | 4 | 1 |
| Th | n.d | 2 | n.d | 3 | n.d | 3 | 1 | n.d | 3 | 2 | 1 | n.d | n.d | n.d | 1 | n.d | 2 | 6 | 1 |
| U | 3 | 1 | n.d | 1 | 3 | 2 | n.d | n.d | n.d | n.d | n.d | n.d | 1 | n.d | 1 | n.d | 1 | 4 | n.d |
| Ba | n.d | 8 | 22 | 14 | 12 | 12 | 11 | 3 | 4 | 1 | n.d | 12 | 1 | 14 | 9 | 4 | 16 | 102 | 7 |
| S | n.d | n.d | n.d | n.d | n.d | n.d | n.d | n.d | n.d | n.d | n.d | n.d | n.d | n.d | n.d | n.d | n.d | n.d | n.d |

APPENDIX *(Cont.)*

| Sample no. | As-11 | As-14 | As-16 | As-21 | As-31 | As-37 | As-65 | As-66 | As-67 | As-69 | As-71 | As-72 | As-75 | As-34A | As-35 | As-36 | As-41 | As-61 | As-63 | As-34B |
|---|---|---|---|---|---|---|---|---|---|---|---|---|---|---|---|---|---|---|---|---|
| Rock | RTM | RTM | RTM | RTM | RTM | RTM | RTM | RTM | RTM | RTM | RTM | RTM | RTM | VNG | VNG | VNG | VNG | VNG | VNG | VNG |
| Major elements (wt %) | | | | | | | | | | | | | | | | | | | | |
| $SiO_2$ | 22.54 | 9.50 | 46.50 | 6.40 | 18.84 | 16.40 | 31.00 | 29.40 | 35.55 | 11.85 | 32.30 | 3.40 | 12.10 | 75.00 | 73.00 | 73.00 | 89.00 | 65.50 | 76.50 | 75.80 |
| $TiO_2$ | n.d | n.d | n.d | 0.01 | n.d | 0.01 | 0.01 | n.d | n.d | 0.01 | n.d | n.d | n.d | 0.01 | 0.05 | 0.08 | 0.02 | 0.02 | 0.11 | n.d |
| $Al_2O_3$ | 0.59 | 0.31 | 0.63 | 1.83 | 0.32 | 4.65 | 0.61 | 0.90 | 0.94 | 2.93 | 2.47 | 0.28 | 1.98 | 8.08 | 9.28 | 13.28 | 3.26 | 9.40 | 4.75 | 12.52 |
| $Fe_2O_3$ | 36.10 | 46.40 | 24.80 | 48.00 | 36.30 | 50.10 | 26.90 | 30.70 | 25.40 | 45.20 | 33.90 | 54.65 | 44.10 | 9.85 | 7.93 | 3.80 | 3.83 | 15.30 | 9.90 | 7.44 |
| MgO | 0.15 | 5.00 | 0.20 | 0.19 | 0.19 | 0.28 | 4.48 | 5.28 | 1.93 | 1.29 | 0.18 | 5.48 | 1.30 | 0.33 | 0.24 | 0.58 | 0.16 | 0.17 | 2.75 | 0.25 |
| MnO | 0.02 | 0.20 | 0.03 | 0.03 | 0.02 | 0.02 | 0.10 | 0.25 | 0.49 | 0.19 | 0.06 | 0.15 | 0.12 | 0.03 | 0.02 | 0.04 | 0.13 | 0.02 | 0.05 | 0.62 |
| CaO | 0.97 | 0.89 | 1.07 | 1.42 | 1.10 | 1.47 | 0.86 | 0.97 | 0.81 | 0.90 | 0.71 | 0.93 | 0.90 | 1.05 | 1.41 | 1.03 | 0.90 | 0.70 | 3.86 | 1.07 |
| $K_2O$ | 0.12 | 0.07 | 0.20 | 0.29 | 0.07 | 1.45 | 0.10 | 0.26 | 0.18 | 0.05 | 0.17 | 0.05 | 0.05 | 3.80 | 3.45 | 5.80 | 0.94 | 4.20 | 0.52 | 0.67 |
| $Na_2O$ | 0.10 | 0.08 | 0.30 | 0.11 | 0.07 | 0.12 | 0.08 | 0.02 | 0.12 | 0.06 | 0.15 | 0.08 | 0.12 | 0.26 | 2.25 | 0.46 | 0.69 | 1.47 | 0.50 | 0.45 |
| $P_2O_5$ | 0.02 | 0.01 | 0.05 | 0.02 | 0.04 | 0.05 | 0.04 | 0.07 | 0.02 | 0.01 | 0.04 | 0.02 | 0.02 | 0.02 | 0.04 | 0.02 | 0.05 | 0.05 | 0.07 | 0.04 |
| LOI | 38.50 | 33.10 | 23.20 | 41.00 | 44.00 | 24.70 | 35.10 | 31.20 | 32.80 | 35.50 | 28.70 | 33.20 | 38.20 | 1.30 | 1.30 | 0.90 | 0.50 | 3.00 | 1.50 | 1.40 |
| Total | 99.11 | 95.56 | 96.98 | 99.30 | 100.95 | 99.25 | 99.28 | 99.05 | 98.24 | 97.99 | 98.68 | 98.24 | 98.89 | 99.73 | 98.97 | 98.99 | 99.48 | 99.83 | 100.51 | 100.33 |
| Trace elements (ppm) except Au (ppb) | | | | | | | | | | | | | | | | | | | | |
| Au | 11,000 | 9,900 | 6,300 | 13,300 | 16,600 | 1,800 | 5,900 | 4,200 | 4,800 | 5,300 | 3,300 | 6,300 | 5,300 | 150 | 50 | 120 | 70 | 60 | 110 | 180 |
| Ag | 6.80 | 8.50 | 6.60 | 12.60 | 6.60 | 3.70 | 18.40 | 16.00 | 17.30 | 22.10 | 173.00 | 14.60 | 104.00 | 1.60 | 0.90 | 0.70 | 0.70 | 4.00 | 1.20 | 1.50 |
| Pb | 316 | 384 | 904 | 327 | 91 | 89 | 2,390 | 3,610 | 5,250 | 310 | 80,500 | 360 | 3,250 | 0 | 30 | 23 | 9 | 210 | 21 | 22 |
| Zn | 265 | 17,065 | 115 | 317 | 24 | 14 | 1,600 | 5,600 | 1,050 | 90 | 4,250 | 255 | 1,360 | n.d | n.d | n.d | n.d | 25 | 47 | 6 |
| Cu | n.d | n.d | n.d | 3,380 | n.d | 0 | 1,180 | 810 | 780 | 60 | 70 | n.d | 1,440 | n.d | n.d | n.d | n.d | n.d | n.d | n.d |
| As | 461,965 | 323,150 | 267,450 | 396,850 | 347,250 | 720 | 101,150 | 72,700 | 71,850 | 268,870 | 156,750 | 441,900 | 128,750 | 895 | 227 | 44 | 92 | 140 | 39 | 20 |
| Sb | 60 | 55 | 90 | 100 | 2 | 2 | 65 | 52 | 51 | 90 | 58 | 20 | 86 | 2 | 2 | 2 | 2 | 2 | 2 | 2 |
| Bi | 42 | 67 | 35 | 58 | 9 | 103 | 68 | 35 | 48 | 65 | 42 | 25 | 63 | 22 | 2 | 25 | 1 | 103 | 7 | 22 |
| Se | 5 | 5 | 3 | 5 | 1 | 5 | 5 | 5 | 5 | 1 | 1 | 1 | 5 | 1 | 1 | 1 | 1 | 1 | 1 | 1 |
| Te | 3 | 3 | 3 | 3 | 3 | 33 | 3 | 3 | 1 | 3 | 3 | 3 | 1 | 7 | 3 | 9 | 3 | 58 | 3 | 7 |
| Cr | 128 | 66 | 263 | 228 | 167 | 160 | 140 | 138 | 126 | 225 | 154 | 67 | 213 | 268 | 333 | 144 | 413 | 235 | 866 | 144 |
| Ni | 82 | 70 | 51 | 116 | 19 | 54 | 88 | 96 | 75 | 45 | 67 | 26 | 54 | 5 | 7 | 6 | 5 | 9 | 133 | 17 |
| Co | 76 | 41 | 155 | 69 | 75 | 89 | 75 | 86 | 84 | 73 | 65 | 17 | 37 | 219 | 157 | 84 | 164 | 113 | 126 | 85 |
| V | 6 | 1 | 4 | 15 | 3 | 17 | 11 | 8 | 16 | 7 | 4 | 1 | 9 | 13 | 4 | 15 | 11 | 7 | 48 | 9 |
| Rb | 2 | n.d | n.d | 10 | n.d | 41 | 2 | n.d | 4 | n.d | 3 | n.d | n.d | 100 | 88 | 180 | 27 | 107 | 9 | 18 |
| Sr | n.d | n.d | 3 | 11 | n.d | 24 | 11 | n.d | 10 | n.d | 2 | n.d | n.d | 58 | 132 | 93 | 44 | 130 | 68 | 352 |
| Zr | 15 | 18 | 15 | 34 | 17 | 46 | 24 | 11 | 19 | 18 | 15 | 16 | 16 | 50 | 58 | 97 | 34 | 27 | 33 | 84 |
| Y | 1 | n.d | n.d | n.d | n.d | 5 | 1 | n.d | n.d | n.d | 1 | 1 | n.d | 6 | 15 | 9 | 5 | 11 | 11 | 22 |
| Nb | 1 | 2 | 1 | 1 | 1 | 5 | 1 | 2 | 2 | 1 | 1 | 2 | 4 | 5 | 10 | 10 | 3 | 9 | 4 | 12 |
| Th | 4 | 24 | n.d | 21 | n.d | 35 | 4 | n.d | n.d | n.d | 4 | 22 | n.d | 10 | 10 | 26 | 3 | 32 | 1 | 24 |
| U | n.d | n.d | n.d | n.d | n.d | 2 | 2 | n.d | n.d | n.d | n.d | 4 | n.d | 2 | 3 | 7 | n.d | 5 | n.d | 4 |
| Ba | 12 | 6 | 8 | 22 | 11 | 154 | 31 | 24 | 14 | 15 | 22 | 12 | 24 | 296 | 266 | 518 | 141 | 569 | 122 | 123 |
| S | 177,600 | 219,150 | 118,350 | 219,750 | 193,350 | 9,750 | 124,650 | 100,950 | 126,550 | 223,540 | 163,580 | 170,200 | 211,550 | n.d | n.d | n.d | n.d | n.d | n.d | n.d |

APPENDIX *(Cont.)*

| Sample no. | As-19 | As-44 | As-42 | As-45 | As-56 | As-2 | As-3 | As-13 | As-25 | As-46 | As-20 | As-06 | As-08 | As-10 | As-15 | As-17 | As-62 |
|---|---|---|---|---|---|---|---|---|---|---|---|---|---|---|---|---|---|
| Rock | VTU | VTU | VTU | VTU | VMU | LRM | LRM | LRM | LRM | LRM | LVM | MSW | MSW | MSW | MSW | MSW | MSW |
| Major elements (wt %) | | | | | | | | | | | | | | | | | |
| $SiO_2$ | 4.30 | 26.40 | 81.5 | 94.00 | 1.8 | 63.11 | 35.82 | 19.22 | 32.6 | 44.5 | 41.80 | 43.12 | 49 | 50.8 | 46.5 | 47 | 52.5 |
| $TiO_2$ | n.d | n.d | 0.06 | 0.01 | n.d | n.d | n.d | n.d | n.d | 0.02 | 0.01 | 0.61 | 0.73 | 0.51 | 0.61 | 0.6 | 0.71 |
| $Al_2O_3$ | 0.84 | 0.90 | 2.4 | 0.80 | 0.3 | 0.73 | 0.43 | 0.79 | 0.81 | 2.3 | 1.04 | 10.1 | 15.3 | 10.8 | 13.6 | 10.5 | 14.8 |
| $Fe_2O_3$ | 42.50 | 30.00 | 4.45 | 2.70 | 24.93 | 7.66 | 38.60 | 37.30 | 15 | 22.6 | 13.82 | 6.39 | 7.66 | 8.25 | 8.82 | 7.16 | 8.5 |
| MgO | 5.58 | 5.48 | 0.3 | 0.73 | 1.17 | 0.31 | 0.14 | 0.36 | 0.75 | 0.77 | 1.84 | 3.23 | 5.27 | 11.25 | 6.49 | 4.5 | 4.55 |
| MnO | 0.02 | 0.01 | 0.08 | 0.01 | 5.72 | 3.66 | 0.17 | 0.29 | 0.14 | 0.01 | 0.25 | 0.1 | 0.11 | 0.13 | 0.13 | 0.17 | 0.17 |
| CaO | 0.91 | 0.76 | 5.85 | 0.70 | 34.51 | 9.98 | 0.93 | 1.86 | 10.9 | 0.07 | 12.60 | 17.59 | 11.3 | 14.51 | 13.6 | 16.5 | 13.7 |
| $K_2O$ | 0.18 | 0.10 | 0.25 | 0.10 | 0.5 | 0.71 | 1.00 | 0.19 | 0.2 | 0.03 | 0.23 | 2.81 | 2.5 | 1.25 | 1.65 | 1.52 | 2.04 |
| $Na_2O$ | 0.07 | 0.09 | 0.07 | 0.09 | 0.22 | 0.11 | 1.13 | 0.10 | 0.08 | 0.09 | 0.11 | 2.15 | 3.6 | 2.55 | 3 | 2.3 | 2.19 |
| $P_2O_5$ | 0.33 | 0.01 | 0.03 | 0.02 | 0.03 | 0.06 | 0.04 | 0.03 | 0.04 | 0.08 | 0.02 | 0.1 | 0.14 | 0.1 | 0.14 | 0.19 | 0.2 |
| LOI | 45.60 | 31.80 | 4.9 | 0.10 | 31.5 | 7.5 | 21.20 | 37.00 | 40 | 25.5 | 27.50 | 10.1 | 1 | 0.4 | 5.8 | 4.7 | 1.2 |
| Total | 100.33 | 95.55 | 99.89 | 99.26 | 100.68 | 93.83 | 99.46 | 97.14 | 100.52 | 95.97 | 99.22 | 96.3 | 96.61 | 100.55 | 100.34 | 95.14 | 100.56 |
| Trace elements (ppm) except Au (ppb) | | | | | | | | | | | | | | | | | |
| Au | 13,500 | 5,100 | 50 | 150 | 350 | 398 | 3,240 | 6,770 | 702 | 220 | 1,200 | 80 | 60 | 440 | 140 | 20 | 20 |
| Ag | 6.70 | 10.20 | 1.2 | 9.80 | 50 | 42.5 | 8.50 | 5.60 | 4.1 | 320 | 3.30 | 1.8 | 1.2 | 0.7 | 1.7 | 1.1 | 1.3 |
| Pb | 106 | 100 | 11 | 15 | 10,100 | 20,240 | 3,790 | 2,480 | 125 | 5,615 | 150 | 20 | 15 | 10 | 39 | 15 | 18 |
| Zn | 45 | 70 | 11 | n.d | 11,920 | 4,720 | 13,530 | 17,060 | 30 | 450 | 45 | 85 | 90 | 87 | 115 | 64 | 106 |
| Cu | n.d | 210 | n.d | n.d | n.d | n.d | 365 | 105 | 12 | 163,675 | n.d | n.d | n.d | n.d | 55 | n.d | 52 |
| As | 496,250 | 389,290 | 198 | 580 | 3,825 | 6,900 | 9,810 | 447,970 | 10,500 | 6,900 | 7,300 | 334 | 46 | 15 | 2,050 | 334 | 14 |
| Sb | 70 | 60 | n.d | 2 | 2 | 290 | 30 | 240 | 2 | 2 | 2 | 2 | 2 | 2 | 2 | 2 | 2 |
| Bi | 44 | 65 | n.d | 1 | 1 | 28 | 1 | 1 | 3 | 107 | 4 | 1 | 1 | 1 | 1 | 1 | n.d |
| Se | 5 | 5 | n.d | 1 | 1 | 1 | 1 | 6 | 1 | 1 | 1 | 1 | 1 | 1 | 1 | 1 | n.d |
| Te | 3 | 3 | n.d | 3 | 3 | 3 | 3 | 3 | 3 | 3 | 3 | 3 | 3 | 3 | 3 | 3 | n.d |
| Cr | 62 | 130 | 612 | 286 | 6 | 202 | 166 | 70 | 28 | 445 | 107 | 306 | 328 | 1,233 | 234 | 295 | 566 |
| Ni | 95 | 80 | 76 | 25 | 14 | 23 | 20 | 70 | 20 | 57 | 31 | 139 | 172 | 572 | 113 | 153 | 186 |
| Co | 46 | 74 | 119 | 5 | 21 | 130 | 83 | 90 | 33 | 81 | 51 | 121 | 110 | 100 | 79 | 88 | 93 |
| V | 4 | 5 | 30 | 10 | 2 | 12 | 4 | 2 | 7 | 38 | 8 | 112 | 169 | 138 | 221 | 134 | 153 |
| Rb | 4 | 1 | 11 | 25 | n.d | n.d | n.d | 5 | 6 | n.d | 7 | 80 | 80 | 48 | 79 | 62 | 27 |
| Sr | 1 | 2 | 16 | 287 | 125 | 42 | 3 | 20 | 89 | n.d | 166 | 227 | 280 | 425 | 290 | 300 | 345 |
| Zr | 18 | 17 | 22 | 31 | 14 | 13 | 13 | 16 | 14 | 25 | 17 | 99 | 116 | 102 | 59 | 92 | 132 |
| Y | n.d | 1 | 10 | 5 | n.d | n.d | n.d | n.d | 3 | n.d | 5 | 20 | 23 | 19 | 16 | 21 | 30 |
| Nb | 1 | n.d | 3 | 5 | 2 | 1 | 1 | 3 | 1 | 2 | 2 | 10 | 10 | 9 | 5 | 6 | 12 |
| Th | 28 | n.d | 1 | n.d | n.d | n.d | n.d | n.d | n.d | n.d | n.d | 5 | 6 | 5 | n.d | 2 | 7 |
| U | n.d | n.d | 3 | n.d | n.d | n.d | n.d | n.d | n.d | n.d | 1 | n.d | 3 | n.d | n.d | n.d | n.d |
| Ba | 13 | 21 | 32 | 199 | 75 | 26 | 8 | 12 | 79 | 57 | 24 | 255 | 330 | 168 | 224 | 171 | 257 |
| S | 215,680 | 192,750 | n.d | n.d | 18,650 | 35,760 | 180,650 | 190,800 | 72,350 | 121,690 | 62,400 | n.d | n.d | n.d | n.d | n.d | n.d |

Abbreviations: MWR = marble wall rocks, RTM = replacement-type mineralization, VNG = vein-type mineralization hosted in the Nikisiani Granite,VTU = vein-type mineralization hosted in the Transitional unit, VMU = vein-type mineralization hosted in the Marble unit, LRM = limonite/Cu hydroxides from RTM, LVM = limonite from VTU, MSW = mica schist wall rocks (Transitional unit), LOI = loss on ignition, n.d = no data